The Astrophysical Journal, 638:1110–1128, 2006 February 20

CURRENT SHEET EVOLUTION IN THE AFTERMATH OF A CME EVENT

A. Bemporad,[1] G. Poletto,[2] S. T. Suess,[3] Y.-K. Ko,[4] N. A. Schwadron,[5] H. A. Elliott,[5] and J. C. Raymond[4]

Received 2005 February 23; accepted 2005 July 26

ABSTRACT

We report on *SOHO* UVCS observations of the coronal restructuring following a coronal mass ejection (CME) on 2002 November 26, at the time of a *SOHO-Ulysses* quadrature campaign. Starting about 1.5 hr after a CME in the northwest quadrant, UVCS began taking spectra at 1.7 $R_\odot$, covering emission from both cool and hot plasma. Observations continued, with occasional gaps, for more than 2 days. Emission in the 974.8 Å line of [Fe XVIII], indicating temperatures above 6×10^6 K, was observed throughout the campaign in a spatially limited location. Comparison with EIT images shows the [Fe XVIII] emission to overlie a growing post-flare loop system formed in the aftermath of the CME. The emission most likely originates in a current sheet overlying the arcade. Analysis of the [Fe XVIII] emission allows us to infer the evolution of physical parameters in the current sheet over the entire span of our observations: in particular, we give the temperature versus time in the current sheet and estimate its density. At the time of the quadrature, *Ulysses* was directly above the location of the CME and intercepted the ejecta. High ionization state Fe was detected by the *Ulysses* SWICS throughout the magnetic cloud associated with the CME, although its rapid temporal variation suggests bursty, rather than smooth, reconnection in the coronal current sheet. The *SOHO-Ulysses* data set provided us with the unique opportunity of analyzing a current sheet structure from its lowest coronal levels out to its in situ properties. Both the remote and in situ observations are compared with predictions of theoretical CME models.

Subject headings: Sun: corona — Sun: coronal mass ejections (CMEs) — Sun: UV radiation

1. INTRODUCTION

Coronal mass ejections (CMEs) involve the catastrophic loss of equilibrium of a magnetic configuration, with the release of the stored energy and a subsequent reconfiguration of the disrupted fields. Independently of the mechanisms that modelers invoke to explain what causes the eruption and to model the field restructuring and accompanying features, there is a general consensus about magnetic reconnection playing a fundamental role in the whole process. Models can be briefly classified either as catastrophe or flux-rope models (see, e.g., Lin & Forbes, 2000) and non–flux-rope models, e.g., breakout (Antiochos et al. 1999) or shearing arcade models (Mikić & Linker 1994). In the latter, reconnection may be the cause of the initial instability and may eventually lead to the formation of a flux rope. In the catastrophe models, a current sheet (hereafter CS) is envisaged, extending from the top of the reconnected loop system to the plasma bubble that surrounds the flux rope: reconnection provides for both the chromospheric and coronal features (separating bright ribbons and growing loop systems) and the interplanetary phenomena (ejection of the plasma bubble). Figure 1 is a cartoon illustrating the flux-rope model of Lin & Forbes (2000).

Direct observations of a CS during a CME event have the capability to contribute relevant information to modelers. However, a CS is supposed to be thin enough to make its detection quite difficult. Moore et al. (1995) infer a thickness of 800–8000 km for the reconnecting "wall" in a large solar flare. Ciaravella et al. (2002) and Ko et al. (2003) assume a CS depth in a post-CME event on the order of $\approx 10^5$ km from the width of a bright, high-temperature emitting region. This size is consistent with the thickness l that can be inferred from the Sweet-Parker relationship $l = hM_A$ (where M_A is the Alfvénic Mach number equal to the ratio of the inflow speed to the local Alfvén speed), assuming a sheet length h of $\approx 5\ R_\odot$ and $M_A = 0.03$, which appears to be the peak value that M_A attains minutes after the CME onset (see Webb et al. 2003 and references therein). This is probably an upper limit to the thickness of the CS, and what is appropriate at later times cannot be easily predicted: while h increases, M_A decreases, and these processes compete in determining the actual size. These values are much larger than those obtained by assuming that the reconnecting region has the typical size of elementary flux tubes (see, e.g., Sturrock et al. 1984), and they show that the CS characteristics are still far from being identified.

Recently there have been reports of CS detections in the extended corona from observations acquired in the wake of CME events by the Ultraviolet Coronagraph Spectrometer (UVCS; Kohl et al. 1995) and the Large Angle and Spectrometric Coronagraph (LASCO; Brueckner et al. 1995) experiments on the *Solar and Heliospheric Observatory* (*SOHO*; see, e.g., Ciaravella et al. 2002; Ko et al. 2003; Raymond et al. 2003). CSs have been identified in UVCS data from the presence of emission from unusually high temperature ions; typically this emission lasts for many hours, although a case for short-lived emission (~minutes) has been presented by Raymond et al. (2003). In the white-light LASCO images, CSs correspond in general to raylike bright structures; similar raylike features have been found by Webb et al. (2003) in *Solar Maximum Mission* data in association with "disconnection events" associated with CMEs and have been ascribed to CSs as well.

In this paper we focus on analyzing the evolution of a CS in the UVCS data in the aftermath of a CME that occurred at

[1] Dipartimento di Astronomia e Scienza dello Spazio, Università di Firenze, Largo Enrico Fermi 5, 50125 Florence, Italy; bemporad@arcetri.astro.it.
[2] INAF–Osservatorio Astrofisico di Arcetri, Largo Enrico Fermi 5, 50125 Florence, Italy; poletto@arcetri.astro.it.
[3] NASA Marshall Space Flight Center, MS SD50, Huntsville, AL 35812.
[4] Harvard-Smithsonian Center for Astrophysics, 60 Garden Street, Cambridge, MA 02138.
[5] Southwest Research Institute, 6220 Culebra Road, San Antonio, TX 78238.

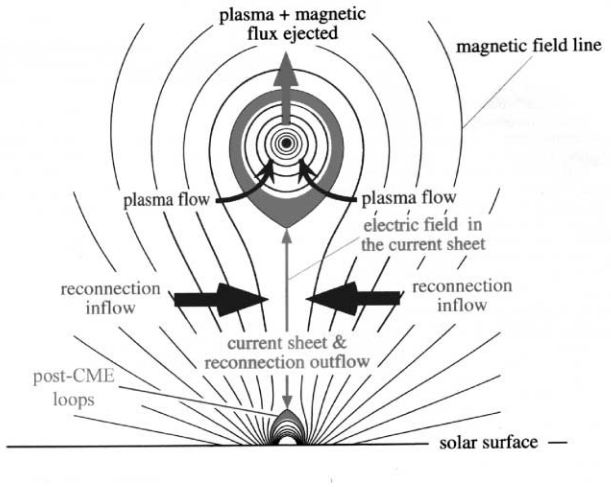

FIG. 1.—CME/flux rope configuration from Lin & Forbes (2000). The position of the post-CME loops (see text) is also shown.

~17:00 UT on 2002 November 26. The existing studies of CME-associated CSs listed above followed the CS evolution over many hours, but provided representative information on the CS characteristics without describing the CS evolution in time. Because the November 26 CS was observed for more than 2 days, we have been able to study its temporal evolution. Order-of-magnitude estimates of flow into the CS and the behavior of the density in the region surrounding the CS are also given.

Ulysses was in quadrature with *SOHO* on November 26 and was directly above the location of the CME observed with UVCS (Poletto et al. 2004). Instruments on *Ulysses* measure the properties of the solar wind plasma (Solar Wind Observations Over the Poles of the Sun [SWOOPS]) and magnetic field (Vector Helium Magnetometer and Fluxgate Magnetometer [VHM/FGM]) and, most importantly, the composition and ionization state (Solar Wind Ion Composition Spectrometer [SWICS]). Although *Ulysses* was far from the Sun at the time, it was possible to identify the CME. We show here that there was a magnetic cloud associated with the CME and that the high ionization state Fe (Fe XVII) was present throughout the magnetic cloud.

In § 2 we illustrate, using LASCO images, the coronal configuration and its changes over 2.3 days, from 2002 November 26 at ≈18:30 UT (when UVCS observations started) up to the time that UVCS observations ended. We also briefly describe the photospheric configuration and the events seen in the *SOHO* Extreme UV Imaging Telescope (EIT; Delaboudinière et al. 1995) over those days. This provides the reader with the overall scenario within which UVCS observations, described in § 3, have been acquired. The method used to infer physical parameters of the CS and adjacent regions, together with the results we obtained, is outlined in § 4. In situ parameters derived from *Ulysses* observations of the coronal plasma ejected in the interplanetary space are described in § 5, and a discussion of our results concludes the paper.

2. THE OVERALL SCENARIO FOR THE 2002 NOVEMBER 26 CME EVENT

In the following, we illustrate the coronal configuration as imaged by the LASCO C2 instrument to help the reader understand the overall scenario of the events occurring during UVCS observations. Prior to the CME, the coronal configuration off the west limb shows two large streamers centered, respectively, at ≈10° (hereafter streamer 1) and 50° north latitude (hereafter streamer 2). The Michelson Doppler Imager (MDI; Scherrer et al. 1995) and the Big Bear Solar Observatory Active Region Monitor (ARM) show on November 26, 24:00 UT the presence of two active region (AR) groups: a northern group, including ARs NOAA 10197 and NOAA 10199 (located respectively at N25W84 and N28W58), and a southern group, including ARs NOAA 10198, NOAA 10201, and NOAA 10195 (located respectively at S18W61, S16W78, and S16W94). This complex configuration (see Fig. 2, *top, and bottom left*) allows for topological connections within individual ARs, as well as for transequatorial loops connecting ARs in the two hemispheres. With respect to the streamer locations, ARs in the northern hemisphere lie on the southern side of streamer 2, and ARs on the southern hemisphere lie on the southern side of streamer 1. The CME we are dealing with started around 17:00 UT on 2002 November 26 in the western hemisphere and was mostly confined within the northwest quadrant. At that time the *GOES* satellite (*Geostationary Operational Environmental Satellite*) did not provide evidence of any large flare event, and it is difficult to identify unambiguously the CME starting time. There are no regions behind the limb that might contribute to the CME: NOAA 10197 and NOAA 10199 are isolated regions in the northern hemisphere, while in the southern hemisphere the closest region to AR 10194 is NOAA 10195, 40° away (and even more distant from the other regions).

In order to check for phenomena occurring in the lower corona, we examined EIT images in the He II λ304 and in the Fe XII λ195 spectral lines. Unfortunately, the 195 Å data have a gap between November 26, 13:13 UT, and November 26, 19:13 UT: the only available EIT data are in He II λ304 and provide no evidence for events from the CME region at the approximate time of the CME initiation. Hence, we have no information on the CME ejection signatures. We note, however, that He II data show, from November 26 through November 29, repeated transient ejections of chromospheric material from streamer 2 (observed by UVCS as a dramatic increase of the C III intensity) unrelated to the CME event; these will be illustrated in a separate paper, Bemporad et al. (2005), and will not be dealt with in this work.

What is relevant for our analysis is the presence of a post-CME loop system, which appears in the 18:36 UT frame in the EIT He II data and is visible for a long time at latitudes ≈20°–30° north (see Fig. 2). The position of the loops supports the hypothesis that EIT is imaging field lines that reconnected after having been torn open by the CME. Figure 2 (*bottom right*) gives the altitude versus time profile of the top of the loops measured from ~18:30 UT: we note that the reconnecting system seems to consist of separate loop subsystems with slightly different characteristics. From a linear fit we derived, for the northern and southern rising loop subsystems, an average speed of about 2.3 and 1.3 km s^{-1}; if we assume these speeds to be constant with time and extrapolate backward, the loop system turns out to start rising at ~12:00 UT on November 26. This time, which is clearly inconsistent with the CME initiation, implies an initial acceleration in the upward loop motion, as predicted by Lin (2002). We notice that the height versus time profile of Figure 2 does not take into account possible projection effects: the loop system appears to bridge over the limb of the Sun, and apparent altitudes may be lower than real altitudes if loops have or have not already rotated beyond the solar limb. Because the northward AR group, where the loops originate, is at the solar limb between November 27 and 29, the heights of the loops can be no more than ≈5% higher than those shown in the plot. This does not sensibly modify the estimate we made of the speed of the rising loop system.

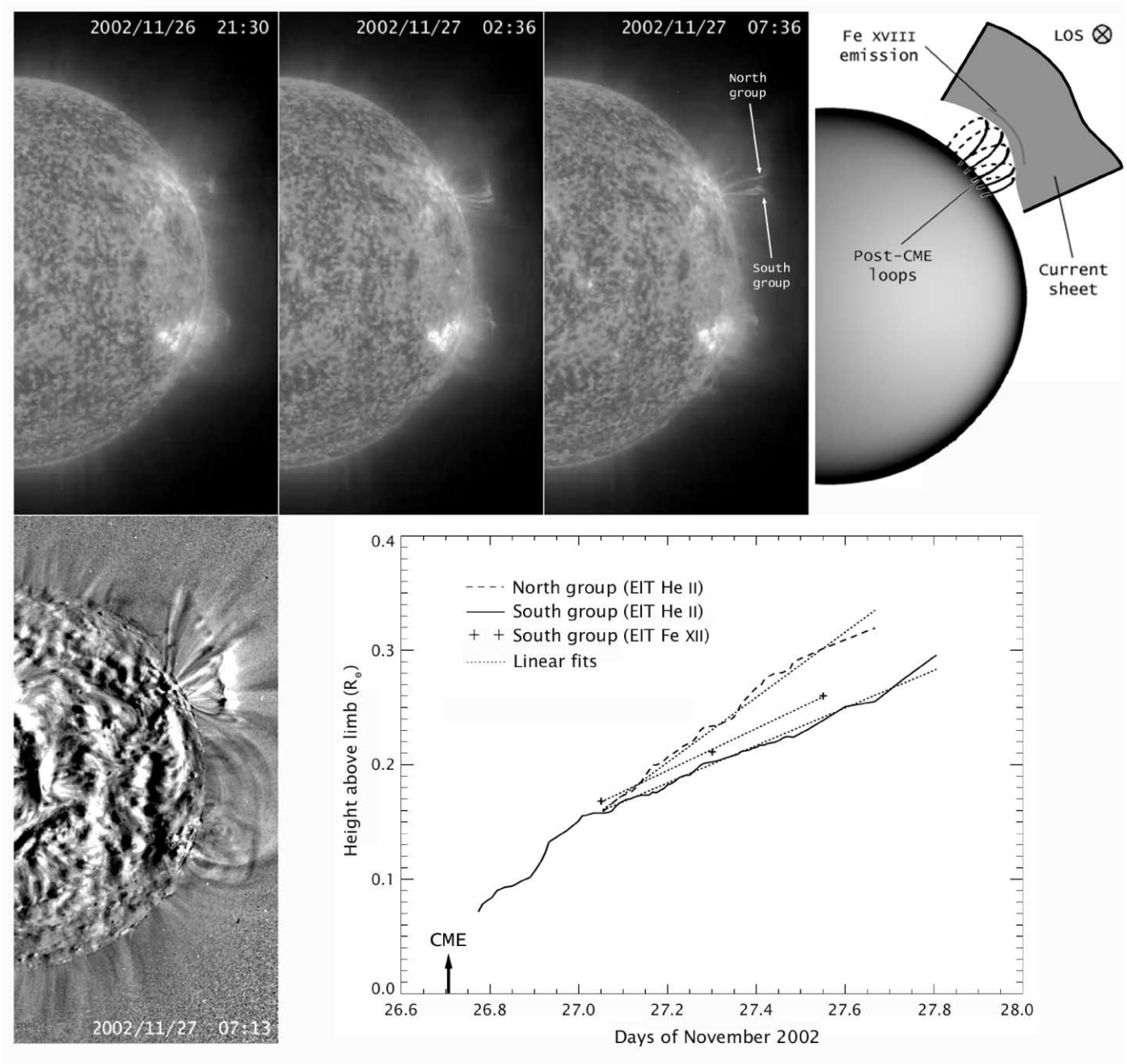

FIG. 2.—*Top*: Images of the loop system developing after the CME, as seen in EIT He II λ304 images at different times. The panel to the right of the EIT images is a cartoon depicting the scenario of the November event at the time UVCS acquired data: the line of sight is normal to a high-temperature region (emitting the hot [Fe XVIII] λ974 spectral line), which we interpret as a CS (see text). The EIT post-CME system consists of loops that bridge over the limb of the Sun. *Bottom left*, An EIT difference image in the Fe XII λ195 emission, which better reveals the bright tops of the reconnecting loops; *bottom right*, altitude vs. time profile of the top of post-flare loops, as measured at different positions and in different lines. The black arrow marks the CME initiation time.

Figure 3 illustrates the white-light coronal activity in the northwest quadrant as seen in images taken by LASCO C2 throughout the 2.3 day observations we made. For future reference, we also show the position of the UVCS slit. As shown in Figure 3, the CME appears to originate from the northward side of streamer 1, between the north and south groups of ARs, and leaves initially the streamer 2 structure apparently unaffected. The relation between the CME and the two AR complexes is not clear. Streamer 1 gets partially disrupted by the CME and deflected by $\sim 7^\circ$ toward southern latitudes. As time goes on, streamer 1 slowly comes back to its original position, and eventually, at the end of our observations (November 29, 02:56 UT), is centered at $\approx 14^\circ$ north (that is, slightly northward of its original position), while streamer 2 shifts by $\sim 6^\circ$ northward as well. However, the multiple cusps at the top of this streamer suggest that we are seeing unresolved substructures that project onto the plane of the sky within the same area. On November 28 at 07:00 UT (see Fig. 3), one of these substructures starts to rapidly shift southward, becoming clearly visible, and, at the end of our observations, is centered at $\sim 30^\circ$ north. This series of events ends up tightening the "gap" area between streamers 1 and 2, which, on November 29, is nearly filled with emitting plasma, making it brighter than it was prior to the CME eruption.

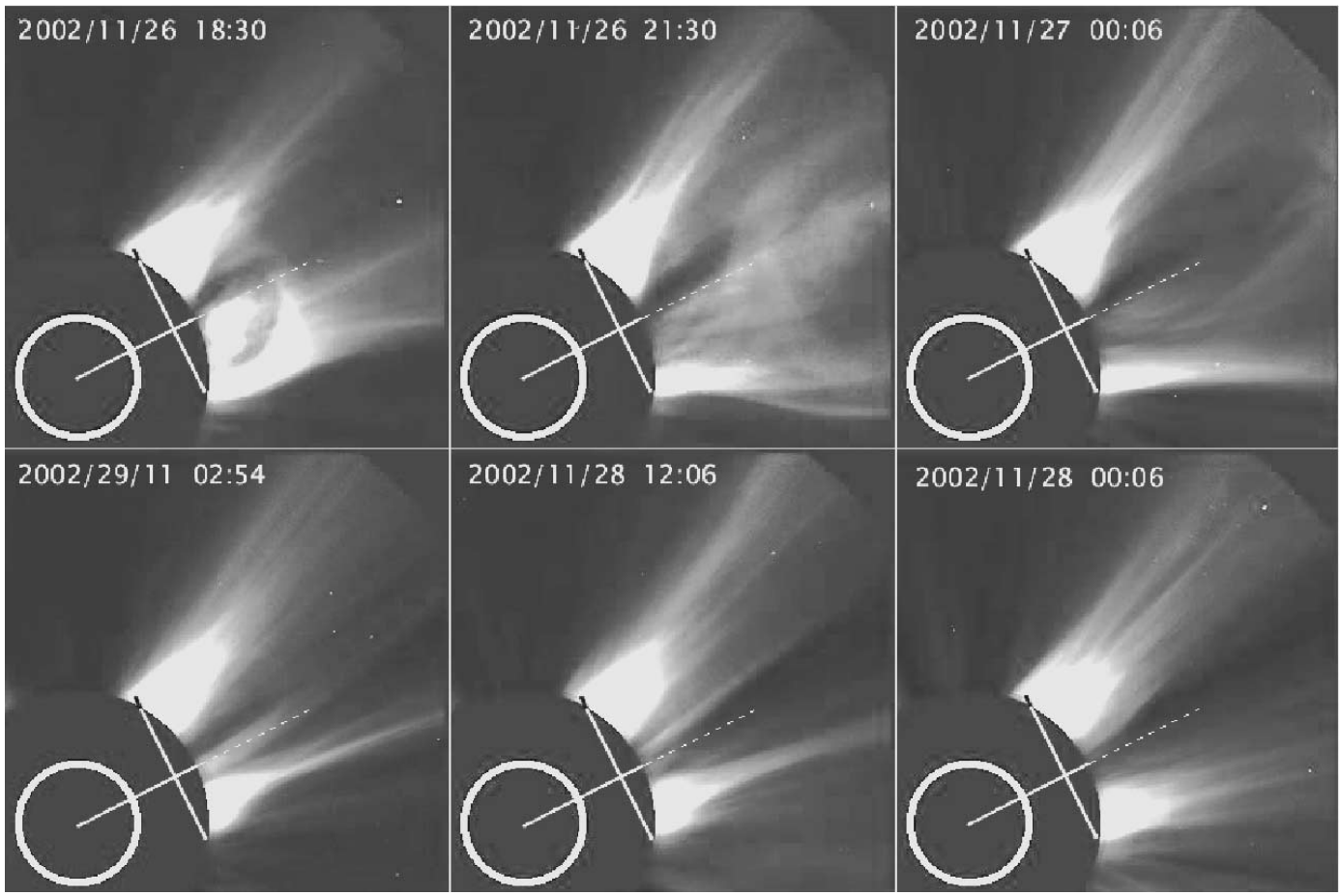

FIG. 3.—LASCO images of the CME event that started on 2002 November 26, ~17:00 UT, at different times (time runs clockwise, starting from the top left panel). Superposed onto the images, we also show the radial direction to *Ulysses* and, normal to the radial, the UVCS slit, centered at 1.7 $R_\odot$ at a latitude of 27° N.

The CME we analyze is not a fast event; this is shown in Figure 4 (*top right*), where we give the variation of heliocentric distance with time for different features within the CME. These plots have been obtained by integrating the different LASCO C2 and C3 frames over the CME extension in latitude (Fig. 4, *top left*) and in heliocentric distance (Fig. 4, *bottom left*) and subtracting the integrated average coronal intensity in the last frame before the CME arrival. As shown by Figure 4 (*top right*), the outward speed varies depending on the different parts of the CME that we consider. In particular, as we derived from a simple polynomial fit of the Figure 4 curves, between 16:54 and 22:06 UT the outward speed of the opening loop preceding the CME core increases from ~90 to ~420 km s^{-1}, while behind the dark cavity, the CME core seems to take off with an initial very low speed that increases up to a final speed that spans between ~130 and ~250 km s^{-1}, depending on the different parts of the CME. As shown by Figure 4 (*bottom right*), the plasma acceleration is still continuing up to heliocentric distances of 15–20 $R_\odot$. Analogous variations in the rising speed of different parts of a CME have been found, e.g., by Lin et al. (2005). Here it is sufficient to notice that, whatever speed is chosen, the November 26 CME is a slowly evolving phenomenon. As shown by Figure 4 (*bottom left*), the CME is slightly deflected along its propagation: this is a consequence of the interaction with the southward streamer 1. The CME, ejected possibly toward southern latitudes from the northward AR group (as shown by the latitude curve), interacts with streamer 1 and promotes the opening of a loop, most probably made up of streamer 1 material, ahead of the CME core; this interaction deflects the CME northward. We now proceed to describe the UVCS observations.

3. UVCS OBSERVATIONS

UVCS observations started on November 26, 18:39 UT, and lasted until November 29, 02:56 UT, with four gaps in between. Because our observations started after the CME ejection, we expect to image the post-CME reconfiguration briefly described in the previous section.

The UVCS slit, normal to the solar radius, has been centered at a northern latitude of 27° in the western quadrant at a commanded altitude of 1.7 $R_\odot$ (see Fig. 3). The slit width was 100 μm, and the detector masks binned the data over 6 pixels (42″) in the spatial direction. The mask has been selected to cover lines from ions originating in hot plasma, as well as from ions originating in cool plasma. Table 1 lists the lines that have been detected during the observations, together with the temperature of formation of the emitting ion from the ionization balance of Mazzotta et al. (1998). The data have a 2 pixel spectral binning (0.1986 Å bin^{-1}) in the 1023.97–1043.23, 998.15–1008.87, and 967.17–981.07 Å spectral intervals and a 3 pixel spectral binning (0.2979 Å bin^{-1}) in the 991.15–994.72 and 943.68–965.13 Å spectral intervals.

The C III λ977.02 emission allows to correct lines for stray light contamination: because the temperature of maximum formation of the C III ion is very low ($T_{\max} \sim 6.3 \times 10^4$ K) with respect to the million degree corona, the presence of this line can be only due to stray light contribution and can be used to estimate the percentage of stray light. Because in our data the C III line is

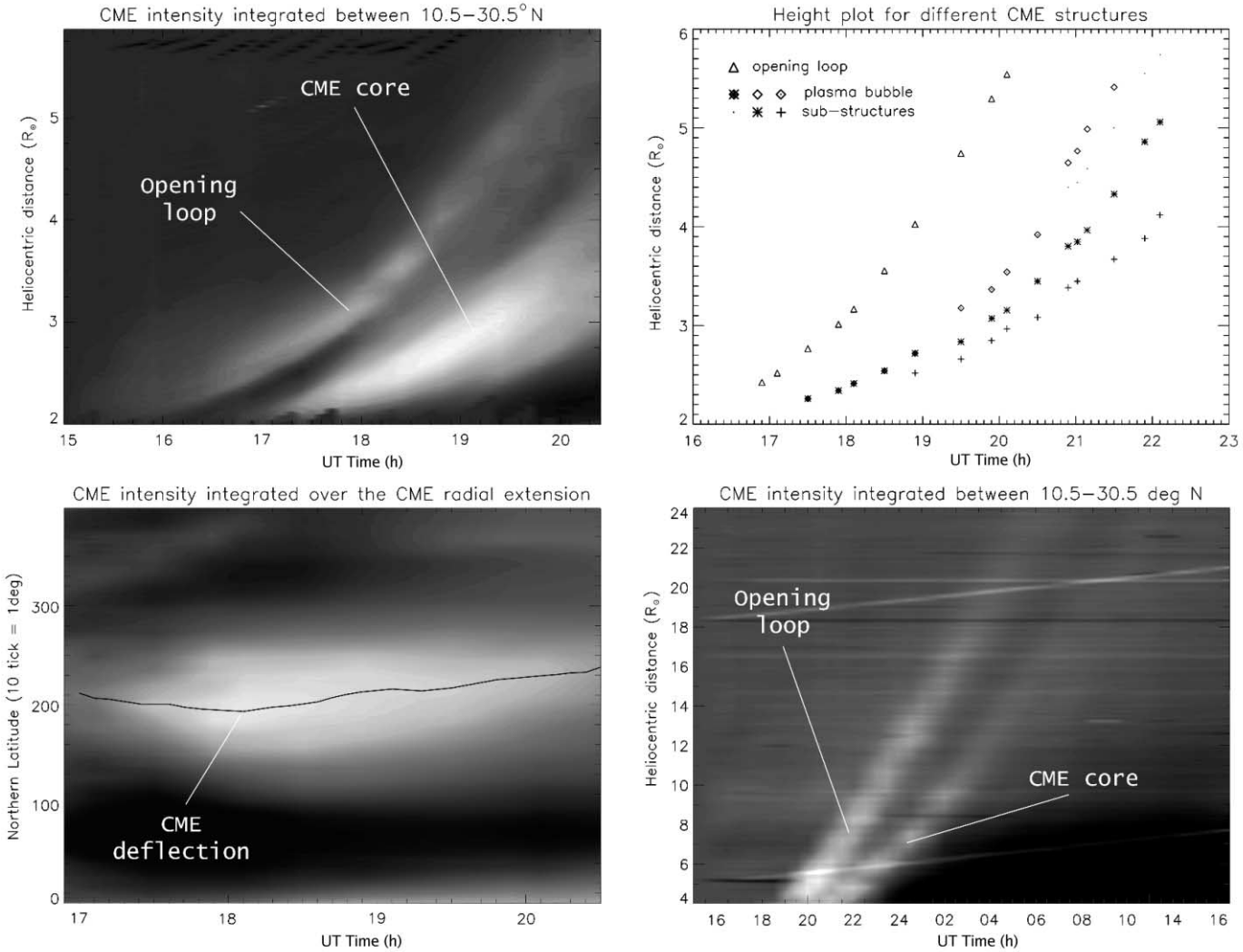

FIG. 4.—Altitude vs. time and latitude vs. time profiles of different CME features at different times on 2002 November 26. *Top left*: Altitude vs. time profile of the CME intensity integrated over the latitude interval between 10°.5 and 30°.5 in LASCO C2 images. *Top right*: Altitude vs. time plot of the top of different CME structures. *Bottom left*: Latitude vs. time profile of the LASCO C2 CME intensity integrated over its whole radial extension, showing a small deflection of the CME toward higher latitudes. Zero on the *y*-axis corresponds to latitude zero; i.e., to the equator. *Bottom right*: Altitude vs. time profile of the LASCO C3 CME intensity integrated over the 10°.5–30°.5 northern latitude interval.

TABLE 1
LINES IDENTIFIED IN THE UVCS SPECTRA

λ_{obs} (Å)	λ_{ID} (Å)	Ion	Transition	log T_{max}
943.66.....	943.61	Ca XIV	$2s^2 2p^3\ ^4S_{3/2}-2s^2 2p^3\ ^2D_{3/2}$	6.5
944.37.....	944.38	Si VIII	$2s^2 2p^3\ ^4S_{3/2}-2s^2 2p^3\ ^2P_{3/2}$	5.9
949.15.....	949.22	Si VIII	$2s^2 2p^3\ ^4S_{3/2}-2s^2 2p^3\ ^2P_{1/2}$	5.9
950.09.....	950.15	Si IX	$2s^2 2p^2\ ^3P_1-2s^2 2p^2\ ^1S_0$	6.0
962.98.....	481.45	Fe XV	$3s\,3p\ ^1P_1-3p^2\ ^1D_2$	6.3
972.51.....	972.54	H I	Lyγ	4.5
974.08.....	487.03	Fe XIII	$3s^2 3p^2\ ^3P_2-3s\,3p^3\ ^5S_1$	6.2
974.77.....	974.86	Fe XVIII	$2s^2 2p^5\ ^2P_{3/2}-2s^2 2p^5\ ^2P_{1/2}$	6.7
976.99.....	977.02	C III	$2s^2\ ^1S_0-2s\,2p\ ^1P_1$	4.8
991.62.....	991.58	N III	$2s^2 2p\ ^2P_{3/2}-2s\,2p^2\ ^2D_{5/2}$	4.9
998.76.....	499.37	Si XII	$1s^2 2s\ ^2S_{1/2}-1s^2 2p\ ^2P_{3/2}$	6.3
1025.69.....	1025.72	H I	Lyβ	4.5
1028.04.....	1028.04	Fe X	$3s^2 3p^4 3d\ ^4D_{7/2}-3s^2 3p^4 3d\ ^4F_{7/2}$	6.0
1031.90.....	1031.91	O VI	$1s^2 2s\ ^2S_{1/2}-1s^2 2p\ ^2P_{3/2}$	5.5
1034.50.....	1034.48	Ni XIV	$3s^2 3p^3\ ^4S_{3/2}-3s^2 3p^3\ ^2P_{3/2}$	6.2
1037.63.....	1037.61	O VI	$1s^2 2s\ ^2S_{1/2}-1s^2 2p\ ^2P_{1/2}$	5.5
1041.04.....	520.66	Si XII	$1s^2 2s\ ^2S_{1/2}-1s^2 2p\ ^2P_{1/2}$	6.3

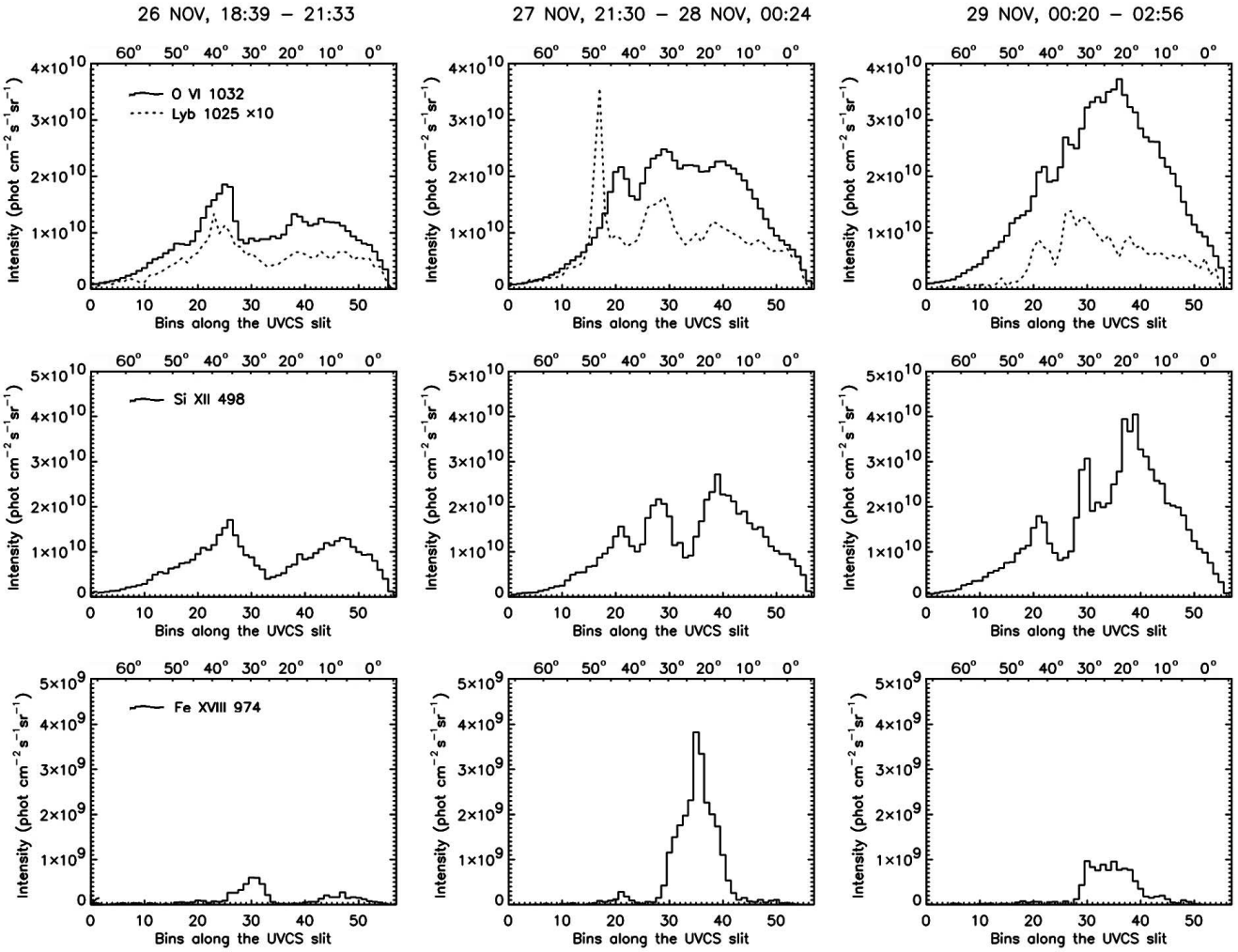

FIG. 5.—Line intensity distribution as a function of the position along the UVCS slit at the beginning of our observations (*left*), an intermediate time (*middle*), and the end of the observations (*right*). Intensities are given in units of photons cm^{-2} s^{-1} sr^{-1} and have been integrated over 9600 s. Selected spectral lines are representative of plasma emitting at progressively higher temperatures (see Table 1 and Fig. 8). *Top*, Intensity along the slit of the O VI λ1032 and of the H Lyβ (multiplied by a factor of 10) lines; *middle*, intensity along the slit of the Si XII λ499 line; *bottom*, intensity along the slit of the [Fe XVIII] λ974 line.

usually not observed at the CME latitudes, this implies that the stray light contribution is negligible.

Figure 5 shows the intensity distribution along the UVCS slit, summed over $\approx$2.5 hr of observations, of four lines, H Lyβ, O VI, Si XII, and [Fe XVIII], that are representative of low, high, and very high temperature plasma. These intensities are given at the beginning of our observations (November 26, 18:39 UT; Fig. 5, *left*), at an intermediate time (November 27, 21:30 UT; Fig. 5, *middle*), and at the end of our observations (November 29, 00:20 UT; Fig. 5, *right*). The Lyβ and Si XII λ499 lines have essentially the same intensity pattern and show brighter emitting features at the position of the northern streamer and of the disrupted southern streamer visible in LASCO images. The gap between the two bright features corresponds to the dark channel between streamers in LASCO images. Synoptic data acquired on November 25 (hence, before the CME) reveal that the O VI and Si XII line intensity distributions were very similar to those observed at the beginning of our observations.

We point out that the EIT rising loop system shows up at latitudes between 20° and 30° north, matching the position of the CME ejection angle. During the same time interval, the [Fe XVIII] λ974 line intensity evolution is completely different: at the beginning of the UVCS observations (Fig. 5, *bottom left*) the emission from this line, as expected, is very weak, if present at all, throughout the whole slit length.[6] In the following days, an enhanced [Fe XVIII] emission, revealing a high-temperature plasma (log $T \sim 6.7$), is concentrated in a wider latitude interval between $\simeq$20° and 30° north; hence, above the EIT rising loop system. Figure 5 shows that at the latitudes of the [Fe XVIII] emission, the low-temperature Lyβ and O VI lines have a local intensity minimum, indicating that these lines are mainly emitted from the low-temperature quiet corona ahead of and behind the hotter region. In the O VI line this behavior is, in the November 26 and 27–28 line panels, less pronounced than that in Lyβ, while on November 29 no minimum appears at the position of the Lyβ dip. This difference can be ascribed (see later on in § 4.1.1) to the O VI line being entirely emitted from the background corona, while the hot region contributes to the Lyβ radiation. In the days after the event, the figure shows the appearance of a third structure between the two streamers: this feature can be identified as

[6] We note that we have no means to ascertain whether the [Fe XVIII] was present or absent at earlier times because the available synoptic data on the previous days do not include this line.

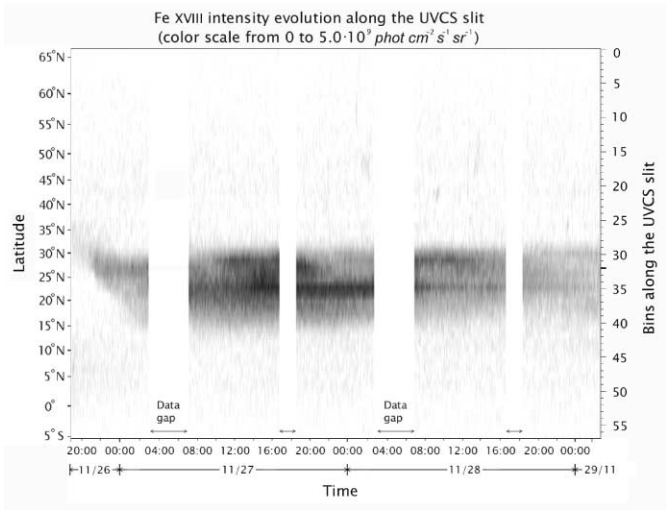

FIG. 6.—Temporal evolution of the [Fe XVIII] λ974 intensity along the UVCS slit. The initial time on this plot (when UVCS observations started) corresponds to the time of the first data point of the bottom right panel of Fig. 4.

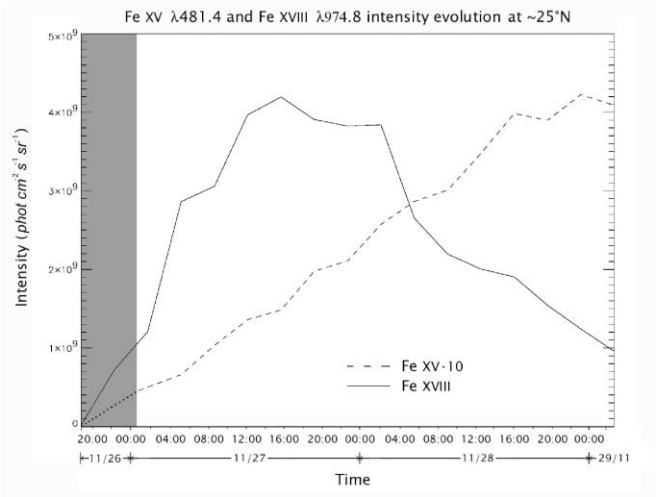

FIG. 7.—Intensity vs. time of the [Fe XVIII] λ974 (*solid*) and Fe XV λ481 (multiplied by a factor of 10; *dashed*) lines at the position of the CS. The Fe XV intensity before November 27, ~00:30 UT (*gray region*) has been extrapolated back from later times (*dotted line*) because the line is too weak (and the statistical errors are too high) to be measured.

the radial structure observed in the LASCO C2 data (see § 2 and Fig. 3, *bottom*). This implies that the hot region at a latitude of about 25° north is included between two approaching features: the northward-moving streamer 1 and the southward-moving radial structure described above.

In order to better understand the evolution of the [Fe XVIII] line emission, we show in Figure 6 the intensity we observed along the UVCS slit during the ~2.3 days following the event, with a time resolution of 240 s. The distribution of the line intensity varies across the 20°–30° north latitude interval, first appearing at northern latitudes and then migrating southward to occupy a wider area. Most of the time the [Fe XVIII] intensity has two emission peaks at ≈22° and 28° north, and these positions remain approximately constant over the 2.3 days of observations. The line intensity, however, shows an increase until the second half of November 28, when it starts decreasing. Outside the high-temperature region, negligible emission in [Fe XVIII] is detected.

A more quantitative view of the evolution with time of the [Fe XVIII] emission is given in Figure 7, which shows the temporal profile of the [Fe XVIII] λ974 and (for comparison) the Fe XV λ481 line intensities, averaged over the 20°–30° north latitude interval (bins 30–37). Spatial averaging allowed us to derive better Fe XV intensities, because, as Figure 7 shows, the 481 Å emission is negligible at the beginning of the observations.

The [Fe XVIII] λ974 emission increases by more than an order of magnitude from November 26, 18:39 UT, to November 27, ~16:00 UT, and slowly decreases afterward. On the other hand, the weak initial emission in the Fe XV λ481 line continuously increases throughout the 2.3 days of observations. Qualitatively, this behavior of the line emission from different ions of the same element can be explained in terms of a temperature *decrease* with time; this is shown in Figure 8, which gives (*left*) the emissivities of the [Fe XVIII] λ974 and Fe XV λ481 lines (and of the [Fe X] λ1028 line, for future reference) versus log T.

In typical coronal conditions (low electron density and high electron temperature), spectral lines form by electron collisional excitation followed by spontaneous emission. In this case, the line emissivity $\epsilon_{\rm line}$ can be defined as

$$\epsilon_{\rm line} \equiv A_{\rm el}\frac{n_{\rm ion}}{n_{\rm el}}(T_e)B_{\rm line}q_{\rm line}(T_e) \text{ photons cm}^3 \text{ s}^{-1}, \quad (1)$$

where $A_{\rm el} = n_{\rm el}/n_{\rm H}$ is the absolute abundance (i.e., relative to hydrogen) of the element whose ion has an ionic fraction $n_{\rm ion}/n_{\rm el}$ (which is a function of the electron temperature T_e) and $q_{\rm line}(T_e)$ and $B_{\rm line}$ are, respectively, the electron excitation rate and the branching ratio for the line transition. The line intensity $I_{\rm line}$ is related to emissivity by

$$I_{\rm line} = \frac{1}{4\pi}\int_{\rm LOS}\epsilon_{\rm line}n_e n_{\rm H}\,dl \text{ photons cm}^{-2} \text{ s}^{-1} \text{ sr}^{-1}, \quad (2)$$

where n_e and $n_{\rm H}$ are, respectively, the electron and proton densities (cm^{-3}) and the integration is along the line of sight (LOS).

Figure 8 shows that the [Fe XVIII] and Fe XV emissivities peak, respectively, at $T \approx 10^{6.7}$ K and $10^{6.3}$ K: hence, if plasma is cooling from a temperature higher than $10^{6.7}$ K, the [Fe XVIII] line emissivity first increases, until that temperature is reached, to decrease afterward, while the Fe XV emissivity continuously increases up to a temperature of $10^{6.3}$ K.

UVCS data have thus revealed the presence of a wide ($\sim 6 \times 10^5$ km) region with anomalously high temperature plasma, which overlies the post-CME loop system imaged by EIT and persists for more than 2 days in the aftermath of the CME. This might possibly originate from the top of the newly reconnected post-CME loops or in the CS formed after the event. Following Ciaravella et al. (2002), Ko et al. (2003), and Raymond et al. (2003), we identify this high-temperature region with the CS that develops in the restructuring corona, as predicted by, e.g., the flux-rope CME model of Lin & Forbes (2000). From here onward, we refer to the bright [Fe XVIII] region as the CS region, and we justify this assumption in § 4.1.1. In the following we concentrate on the temporal evolution of the CS physical parameters, averaged over the ~20°–30° north latitude interval.

We note that post-CME loops (as shown in Fig. 2) seem to bridge over the solar limb: hence, we expect to see the CS, which lies approximately in the plane of the sky (Fig. 2, *top right*), face-on. As a consequence, emission along the LOS originates both in the CS and in the "quiet" coronal plasma ahead of and behind it, and the temperatures, densities, and element abundances of the CS and of the intervening quiet coronal regions may be different. In order to derive the CS parameters, it is mandatory to separate

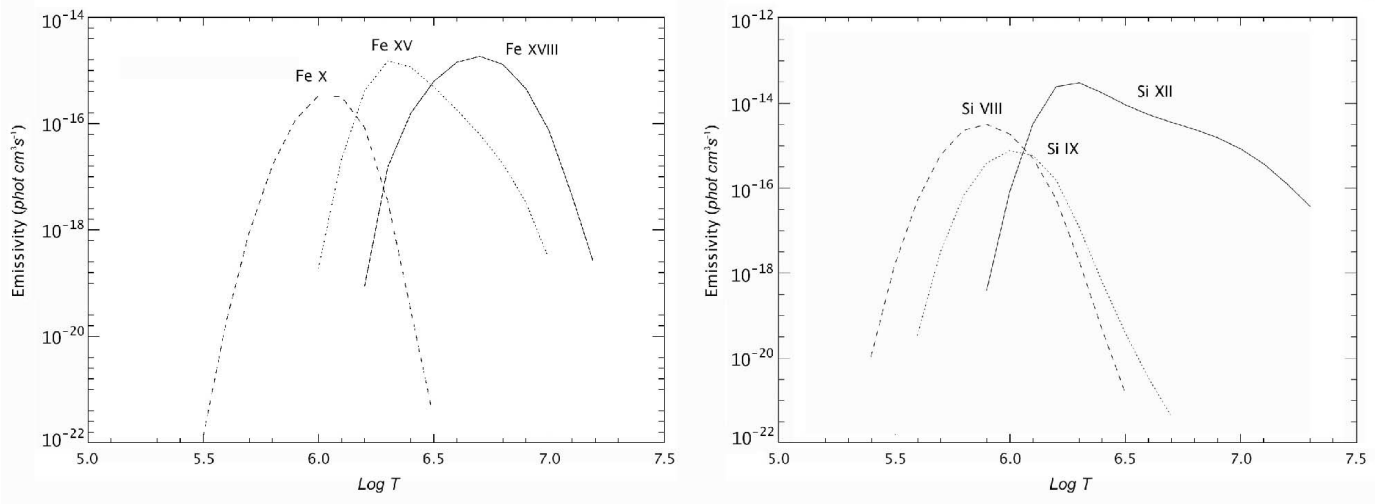

FIG. 8.—Emissivities of the [Fe x] λ1028, Fe xv λ481, and [Fe xviii] λ974 lines (*left*) and of the [Si viii] λ944, [Si ix] λ950, and Si xii λ499 lines (*right*) from the CHIANTI spectral code (ver. 4.2), based on the ionization equilibria of Mazzotta et al. (1998).

the CS and the coronal contribution along the LOS: at the latitude of the CS, both regions contribute to the observed line intensities, while at the latitudes beside the CS, only the quiet coronal emission is present. In the following, we describe the techniques by which these contributions have been identified, and we derive the temporal evolution of parameters within the CS and in the quiet coronal regions.

4. PHYSICAL PARAMETERS IN THE CORONA AND IN THE CURRENT SHEET

For clarity, we hereafter illustrate the methods used to evaluate temperatures, elemental abundances, and densities in the CS and ambient corona and give the results inferred from the data immediately after different techniques have been described. Often individual results are interrelated, and we give in the Appendix (see Fig. 18) a flowchart diagram that shows the links between different steps in our procedure. We like to point out that ionization equilibrium has been implicitly assumed to hold throughout our calculations. The validity of this assumption will be discussed in § 6.

4.1. *Electron Temperature Diagnostics*

Electron temperatures are usually derived from the intensity ratios of lines from different ions of the same element, under the assumption that they originate in the same isothermal plasma. The emissivity curves of Figure 8, however, show that plasma emitting in the [Fe x] λ1028 line has too low a temperature to account for the [Fe xviii] λ974 line, which forms only at high temperatures, while the Fe xv λ481 line originates from an intermediate regime to which both the low- and high-temperature plasmas may contribute. At the position of the CS, where the [Fe xviii] emission is detected, emission from a quiet, low-temperature corona is superposed along the LOS onto the high-temperature emission from the CS. Hence, temperatures cannot be derived simply from the observed Fe line intensities, because, independent of the pair of lines we choose ([Fe x] λ1028 and Fe xv λ481 or [Fe xviii] λ974 and Fe xv λ481), we end up mixing contributions from different plasmas.

In order to derive the electron temperature of the quiet corona along the LOS, we then resort to [Si viii] λ944 and [Si ix] λ950 line emission, as their peak emissivities are in the $5.9 \leq \log T \leq 6.0$ temperature range typical of the quiet corona (see Fig. 8, *right*, and Table 1). Once the value of the electron temperature of the quiet corona is determined from the Si line intensity ratio, we derive with this value and the observed [Fe x] line intensity (see eqs. [1] and [2]) the factor $E_{\rm Fe} = A_{\rm Fe} n_e n_{\rm H} L$, where L is the thickness of the emitting low-temperature plasma along the LOS. If we know T_e and $E_{\rm Fe}$, we can calculate the contribution $I_{\rm Fe\,xv,\,QC}$ to the Fe xv line emission originating from the quiet corona and, by subtracting this contribution from the observed line intensity, derive the contribution from the CS region $I_{\rm Fe\,xv,\,CS}$ to the total line emission. Because the [Fe xviii] is emitted only from the high-temperature plasma in the CS, the ratio between the intensity of the [Fe xviii] λ974 line and the $I_{\rm Fe\,xv,\,CS}$ line component gives an estimate of the CS electron temperature. Note that this procedure avoids making any hypothesis on the value of the Fe abundance in the CS, which is possibly different from the Fe abundance in the quiet corona; however, we made the simplifying assumption that the quiet corona and the CS plasma are both isothermal.

4.1.1. *Electron Temperatures in the Current Sheet and Adjacent Regions*

We illustrate now the results obtained by applying the technique described in § 2 to our data set. We first examine the electron temperature evolution in the quiet corona.

Figure 9 shows the behavior of the electron temperature along the UVCS slit at different times. Scatter between individual points is due to uncertainties in the [Si viii] and [Si ix] line intensities (both are blended with other lines; see later in this section), which has been minimized by averaging over 9600 s. In spite of the uncertainties, however, a value of $\log T \sim 6.25$ for regions at either side of the CS is clearly defined. The regions that border the CS, hence, the regions beside the area where the CME occurred, are occupied by streamers. Because $\log T \sim 6.25$ is the temperature of maximum formation of the Si xii ion (see Fig. 8), we expect each streamer to correspond to a peak in the [Si xii] emission; this is confirmed by Figure 5.

A temperature of $\approx 10^{6.2}$ K is in agreement with estimates of temperatures in streamers at comparable heights. For instance, Uzzo et al. (2004), from UVCS data, found T_e ranging in $6.1 \leq \log T \leq 6.3$ for AR streamers observed in 2001. Parenti et al. (2000) and Bemporad et al. (2003), for streamers observed, respectively, in 1998 and 2000, found electron temperatures on the

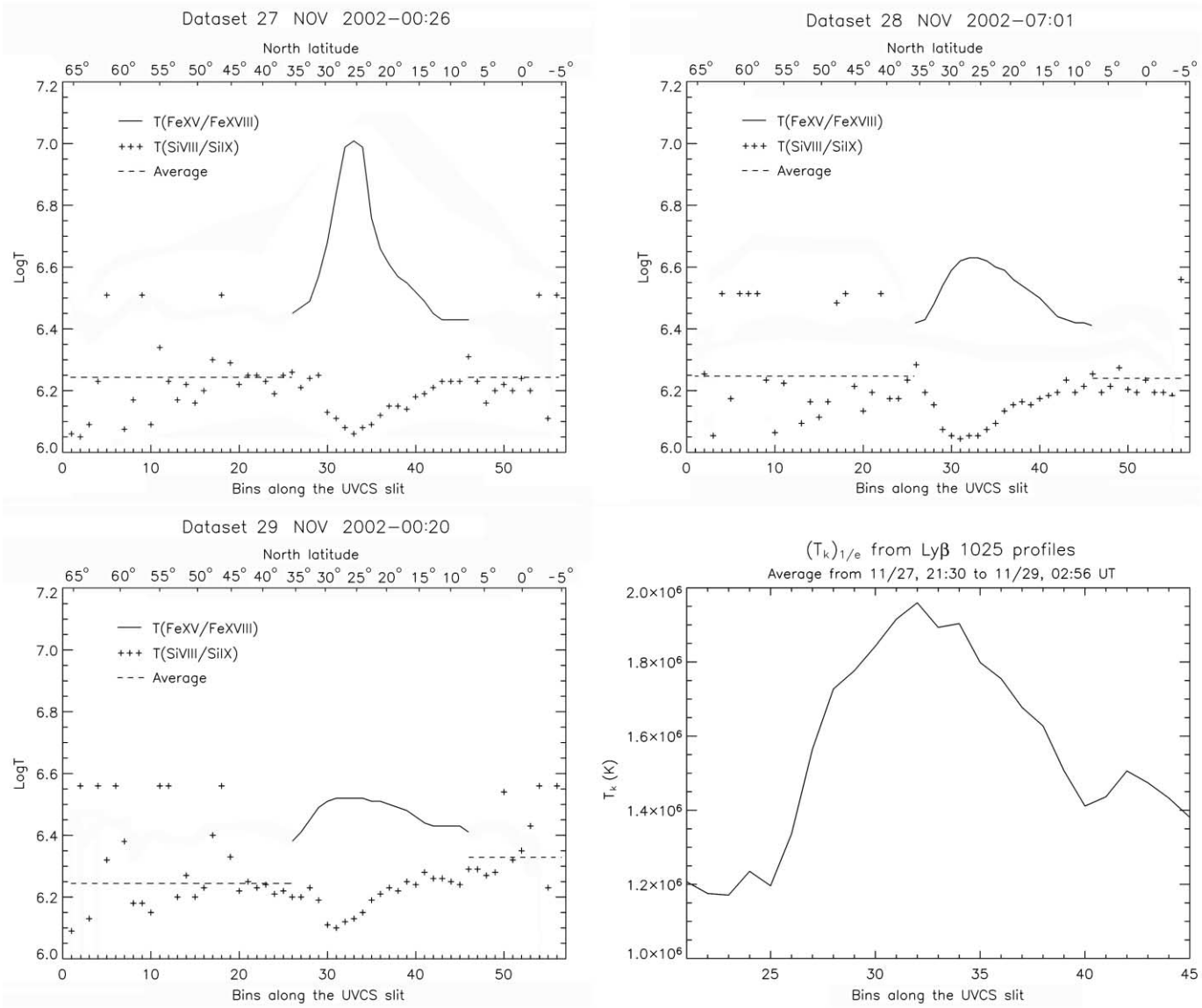

FIG. 9.—*Top left, top right, and bottom left*: Electron temperatures (*plus signs*) along the UVCS slit from the ratio between lines from Si VIII and Si IX ions at representative times on November 27, 28, and 29. Bins along the UVCS slit are given in the abscissa; corresponding heliographic latitudes appear at the top of each panel. The solid line gives the CS temperature from the ratio of [Fe XVIII] to the fraction of the Fe XV line emission that originates from the CS. Outside the CS, where [Fe XVIII] emission is missing, the average temperature from individual determination is indicated by the dashed line. *Bottom right*: Kinetic temperatures from the Lyβ line profiles along the UVCS slit (at CS latitudes) averaged over $\sim$30 hr of observation.

order of 10^6–$10^{6.15}$ K at altitudes ranging between 1.5 and 1.9 $R_\odot$, still from UVCS data. Foley et al. (2002) from Coronal Diagnostic Spectrometer (CDS) data derived a slightly higher temperature of $\approx 10^{6.34}$ K at 1.6 $R_\odot$ for streamers observed near solar maximum.

Over the latitude interval where the high [Fe XVIII] emission shows up, the temperature from the [Si IX]/[Si VIII] ratio has a minimum that reveals the quiet corona beside the CS latitudes to have different physical properties than the corona along the LOS ahead of and behind the CS. Lower temperatures along the LOS at the CS position can be ascribed to plasma left over by the CME rather than to the streamer plasma on either side of the CS.

This temperature dip at the CS latitude originates in the observed [Si VIII] and [Si IX] line intensity variation in the transition from the CS ($\sim 25^\circ$ north) to adjacent latitudes (see Fig. 10, *left*). Although the Si line intensities reach maximum at the CS latitudes, it is their ratio that indicates the temperature dip. Moving away from the CS, the [Si VIII]/[Si IX] ratio decreases; this implies higher temperature, because the T_e increase we derived from the CS to adjacent latitudes corresponds to a decrease in the [Si VIII] and [Si IX] line emissivities (see Fig. 8), respectively, by factors of $\sim$40 and $\sim$8.[7]

The low value in correspondence of the CS does not show any appreciable change over the 2.3 days of our observations. This is illustrated by Figure 10 (*right*): because the electron density increases with time (see § 4.3.1), the [Si VIII] and [Si IX] line intensities increase, but their ratio stays approximately constant, giving a constant quiet corona temperature. Figure 10 also shows that the [Si VIII] $\lambda\lambda$944.4, 949.2 doublet lines are blended, respectively, with the [Ca XIV] λ943.6 and [Si IX] λ950.1 lines, leading to uncertainties in the line intensity determination. The ensuing errors in the temperature evaluation are discussed at the

[7] This is not the case for the O VI λ1031.91 line, whose emissivity decreases by only a factor of $\sim$2; see Fig. 5.

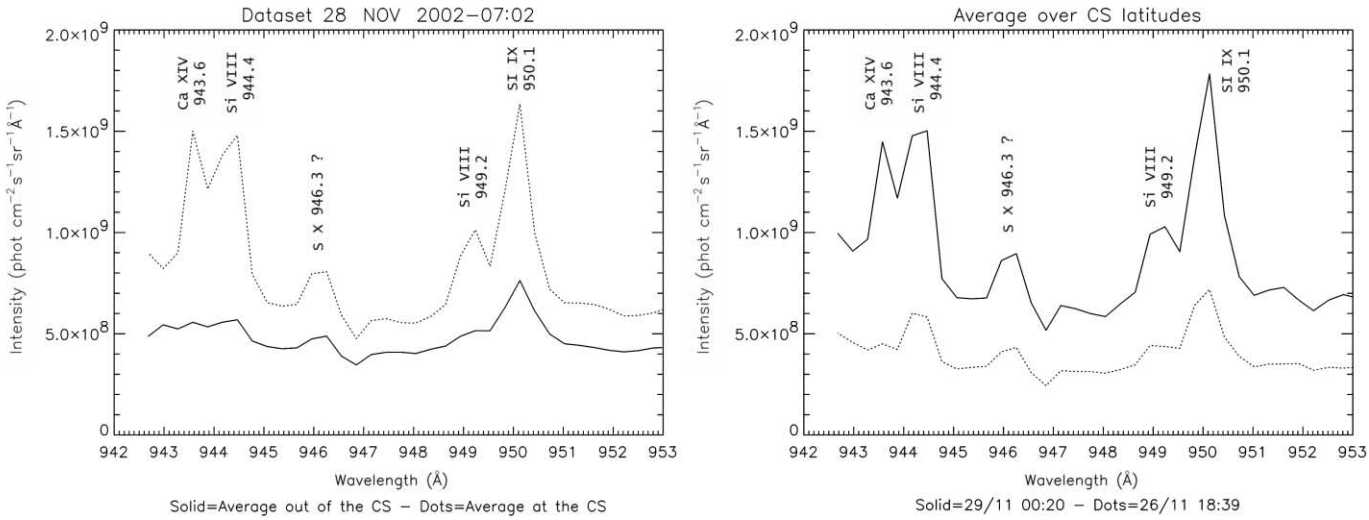

FIG. 10.—*Left*: Representative behavior of the [Si VIII], [Si IX], and [Ca XIV] spectral lines at the CS (*dotted line*) and out of the CS (*solid line*). Data have been averaged over ~2.6 hr starting on November 28 at 07:02 UT, over bins 30–37 for the CS latitudes, and over all the residual bins for the adjacent region. *Right*: Representative spectra at the CS latitude (bins 30–37) integrated over ~2.6 hr at the beginning (November 26; *dotted line*) and at the end (November 29; *solid line*) of our observations.

end of this section. We point out that emissivities from the O VI lines decrease by about 2 orders of magnitude as T_e increases from the $\approx \log T = 6.0$ of the quiet corona to the $\approx \log T = 6.6$ of the CS; hence, the CS has too high a temperature to contribute to the O VI emission.

In order to derive the CS temperature evolution, we need to resort to the ratio between the [Fe XVIII] line and the component of the Fe XV line originating in the CS. Figure 9 (*solid line*) shows the evolution along the UVCS slit of the resulting CS temperatures. A comparison between Figures 6 and 9 shows that a single peak in the CS temperature often corresponds to two peaks in the [Fe XVIII] line intensity at latitudes of ~22° and 28° north. This is a consequence of the [Fe XVIII] emissivity changing along the slit as temperature decreases northward and southward of the latitude of ~25° north. The occasional disappearance of one of the [Fe XVIII] λ974 intensity peaks may be ascribed to reconnection processes involving at different times loops located at different latitudes. Although the altitude and time difference between EIT and UVCS observations does not allow us to establish a close correspondence between what is seen by the two instruments, EIT images show a spatially intermittent brightening of loop tops, indirectly supporting UVCS evidence.

Figure 9 (*bottom right*) gives the kinetic temperatures T_k of the Lyβ line along the UVCS slit, which is consistent with the CS temperature profiles shown in the other panels. Kinetic temperatures have been crudely evaluated from Gaussian fits of the observed Lyβ profiles. Because the Lyβ line originates from both the CS and the quiet corona along the LOS, we expect at CS latitude a Lyβ T_k increase weaker than the temperature increase inferred from the [Fe XVIII]/Fe XV ratio. This is confirmed in Figure 9 (*bottom right*) by the factor of ~2 variation in the Lyβ value of T_k.

Figure 11 presents the temporal evolution of the average CS temperature: data have been accumulated over the CS latitude interval (bins 30–37). Initially (Fig. 11, *gray region*), because the observed intensity of the Fe XV line is negligible (see Fig. 7), we cannot give a reliable estimate of the CS temperature. The weak Fe XV emission can be explained by the quiet corona temperature behind and in front of the CS ($\log T \sim 6.05$–6.10) and the CS temperature ($\log T \geq 6.9$), which is at either side of the temperature maximum ($\log T = 6.3$) of the Fe XV line emissivity.

A $\geq$50% decrease in the temperature of the sheet occurs over the 2.3 days of observations, hinting at the CS cooling. The increase with time of the [Ca XIV] λ943.6 line intensity (see Fig. 10, *right*) supports this conclusion, because the CS cools down, approaching the temperature of maximum [Ca XIV] line emissivity (see Table 1). There have been previous detections of [Ca XIV] in CSs: for instance, Ko et al. (2003) observed both the [Fe XVIII] and [Ca XIV] lines but could not reproduce their intensities other than by invoking the CS to spread over a range of temperatures ($6.46 \leq \log T \leq 6.66$). Possibly this depends on the different orientation of the Ko et al. (2003) CS, which was seen edge-on: hence, different temperatures could align along the LOS. A multitemperature CS can be envisaged if either reconnection is going on with different characteristics at different positions (for

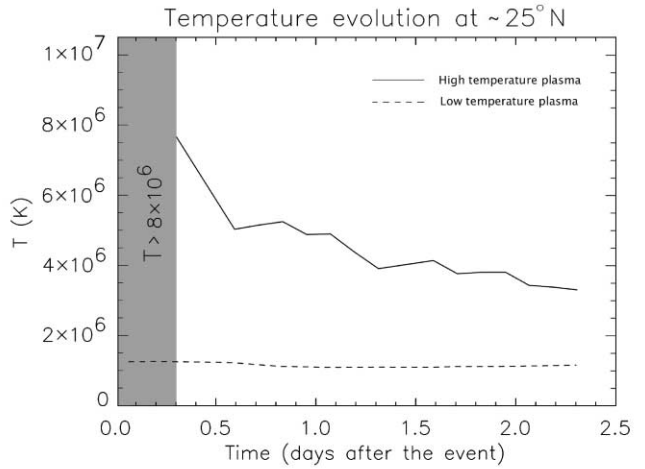

FIG. 11.—Evolution of the CS temperature (*solid line*) over ≈2.3 days from the ratio between the observed [Fe XVIII] line intensity and the calculated CS intensity of the Fe XV line. Because the latter is negligible and cannot be evaluated in earlier data (*gray region*), temperatures can only be assumed to be higher than 8×10^6 K. Temperatures from the [Si VIII]/[Si IX] line ratio at the CS latitude are also shown (*dashed line*).

instance, the reconnecting magnetic field strength varies along the reconnection region) or the reconnection process started at different times at different positions along the reconnecting arcade. In both cases, integrating along the CS implies integrating through an inhomogeneous CS.

The CS temperature evolution described above allows us to check the assumption we made that the high-temperature [Fe XVIII] emission seen by UVCS originates from the CS and not from the cusps of the post-CME rising loops. Order-of-magnitude estimates of the conductive and radiative cooling times for a semicircular loop of height of $0.7\,R_\odot$ show that the loops cool mainly by conduction over times on the order of 1 hr. This short time is clearly incompatible with the very slow temperature decrease shown in Figure 11. Moreover, with the low rising speeds derived from EIT images (see Fig. 4), the post-CME rising loops would arrive at the UVCS slit height of $0.7\,R_\odot$ over the solar limb only 2–3 days after the event. This led us to conclude (in agreement with Ciaravella et al. 2002, Ko et al. 2003, and Raymond et al. 2003) that the high-temperature plasma we detected originated from the CS.

Before concluding this section, we discuss the errors in the procedures described above. As we anticipated, both the [Si VIII] and [Si IX] spectral lines are blended with other lines, and this may affect the determination of the quiet corona temperature: in particular, the [Si VIII] λ944.37 line is blended with the [Ca XIV] λ943.61 line. Because the emissivity of [Ca XIV] peaks at a temperature of $\log T = 6.5$ (see Table 1), its emission is usually negligible outside the CS. Hence, outside the CS, the [Si VIII] line intensity is not blended with the [Ca XIV] line. At the CS latitudes the temperature of $\log T = 6.5$ is reached only at the end of our observations: at these late times the increased [Ca XIV] emission may lead to an overestimate of the [Si VIII] intensity by $\leq$40%. If we take into account this error, the derived temperature may increase by no more than 0.1 dex, possibly indicating that $\sim$2 days after the CME, the dip in the quiet corona temperature visible in Figure 9 at the CS position starts disappearing.

A further problem we need to solve is the blend of the [Si IX] λ950.15 and [Si VIII] λ949.22 spectral lines. However, we solved this problem by taking into account that the ratio between the intensities of the [Si VIII] $\lambda\lambda$944.38, 949.22 doublet lines is 2. We then subtracted from the observed [Si IX] λ950.15 and [Si VIII] λ949.22 blend one-half of the [Si VIII] λ944.38 intensity.

Errors in the CS temperature determination depend mainly on the [Fe XVIII] and Fe XV observed intensities and on the separation between the fraction $I_{\mathrm{Fe\,XV,\,CS}}$ of the Fe XV intensity emitted from the CS and the fraction $I_{\mathrm{Fe\,XV,\,QC}}$ emitted by the quiet corona. The latter depends on the quiet corona electron temperature $T_{e,\,\mathrm{QC}}$ derived from the [Si VIII]/[Si IX] ratio, and we said this might possibly be underestimated by up to 0.1 dex. However, the error in the temperature of the quiet corona ahead of and behind the CS needs to be lower than 0.1 dex, because an increase that large yields a Fe XV line emission larger than that observed. Assuming, for instance, the value of $T_{e,\,\mathrm{QC}}$ to be higher by 0.02 dex does not sensibly modify the CS temperatures beyond November 27, 07 UT. At earlier times, because this higher value of $T_{e,\,\mathrm{QC}}$ results in a higher value of $I_{\mathrm{Fe\,XV,\,QC}}$ fraction (i.e., a lower value of $I_{\mathrm{Fe\,XV,\,CS}}$), the CS temperature would be higher than that shown in Figure 11. Statistical errors in the observed Fe XV intensity go from $\geq$90% at the beginning of our observations down to $\sim$10% on November 29 (because of the continuous increase in the Fe XV intensity), while statistical errors in the observed [Fe XVIII] intensity are between 5% and 15%. In conclusion, the CS temperature is accurately inferred after November 27, 07 UT, while at earlier stages only a lower minimum to the real value of T_e can be given.

4.2. *Elemental Abundance Diagnostics*

Having derived the electron temperatures of the quiet, low-temperature corona and of the high-temperature CS that contributes to the LOS emission, we proceed to determine element abundances in both regions. As a premise, we remind the reader that spectral lines emitted also at chromospheric temperatures, such as H and O VI lines, are formed at coronal levels both by collisional and radiative excitation. Absolute element abundances A_{el} can be derived from the collisional components of lines, provided that the collisional component of a hydrogen line is also known. In this case, under the assumption that the collisional components of both lines originate in the same region, we write

$$A_{\mathrm{el}} = \frac{E_{\mathrm{el}}}{E_{\mathrm{H}}}. \tag{3}$$

In the present data set, we detected both the H Lyβ and Lyγ lines. In order to identify the collisional and radiative components of the hydrogen lines from their observed intensities, we followed a standard procedure (see, e.g., Raymond et al. 1997). Because excitation rates are known, one can easily predict the ratios between the radiative (independent of temperature) and collisional (weakly dependent on temperature) components of the Lyman lines. The observed intensities and the predicted ratios allow the identification of the components of the lines. Usually, this procedure is applied to the Lyα and Lyβ lines: in our case, because Lyα is not included in our data, we used the Lyβ and Lyγ lines. Then from the known electron temperatures of the CS and of the quiet corona, the percentage contribution of these regions to the collisional intensities has been inferred (as done for the $I_{\mathrm{Fe\,XV}}$ line), their E_{H} factors have been estimated, and abundances A_{el} have been calculated from equation (3).

4.2.1. *Elemental Abundances in the Current Sheet and Adjacent Regions*

We examine here the behavior of O, which is a high first ionization potential (FIP) element, and of Fe and Si, which are low-FIP elements; abundances of these elements are given in Figure 12. The oxygen abundance can be derived only for the regions external to the CS, because, as already mentioned, the CS has too high a temperature to contribute to the O VI emission. Errors in the abundance values are easily on the order of $\pm$0.1 dex for O abundances and of $\pm$0.2 dex for Fe and Si abundances; this error can be ascribed mainly to uncertainties in the identification of the Lyβ collisional component (which affects all abundances in the same way) and in the estimate of line intensities (more difficult for second-order lines). Hence, the apparent increase in the oxygen abundance with time, seen in Figure 12 (*top left*), is within the uncertainties of the measurements and cannot be confirmed. Even so, oxygen appears to be depleted with respect to its photospheric abundance [$\log N(\mathrm{O})_{\mathrm{phot}} = 8.82$; Allen 1973], an effect that can easily be explained if we envisage the quiet plasma ahead of and behind the CS to be the remnant of the streamer that has been partially disrupted by the CME event. An oxygen depletion in streamers has been found by many authors (see, e.g., Raymond et al. 1997; Uzzo et al. 2003; Bemporad et al. 2003); hence, we can interpret the present underabundance to be a signature of the streamer origin of the plasma that is being sampled.

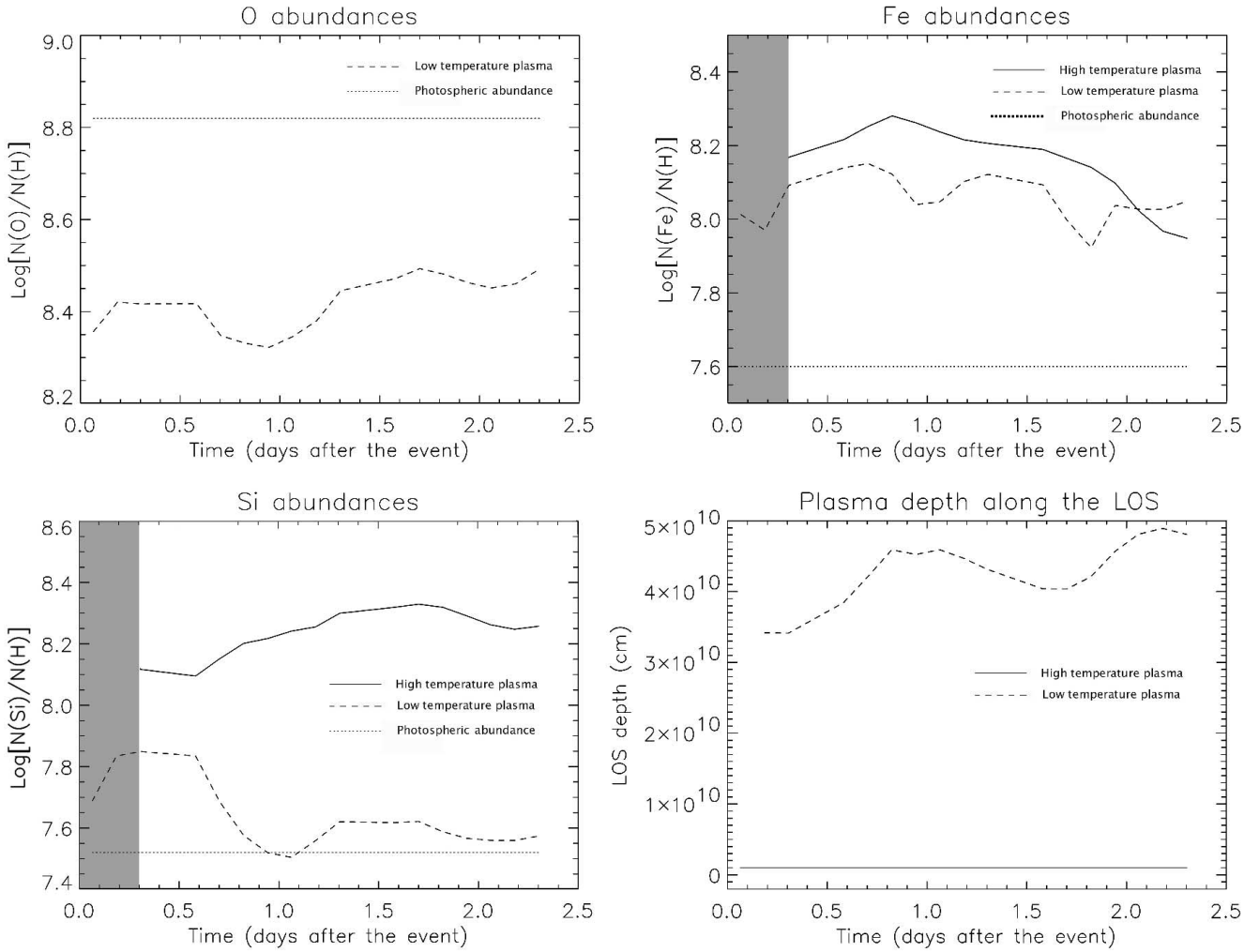

FIG. 12.—*Top left*: Oxygen abundance in the quiet corona at the location of the CS vs. time (*dashed line*) over the 2.3 days of observation. The straight dotted line gives the assumed photospheric abundance. *Top right*: Same as for the top left panel; the dotted line gives the Fe abundance in the CS. *Bottom left*: Same as the above panels, but for Si. *Bottom right*: The assumed CS thickness l (*solid line*) and the computed quiet corona thickness L (*dashed line*) along the LOS. A gray region covers times when uncertainties are too high to give reliable CS elemental abundances.

We note that the oxygen abundance can also be derived from the ratio between the O VI and Lyβ radiative components (see, e.g., Raymond et al. 1997). Because of the different dependence of the radiative and collisional components of the line on n_e, abundances derived from radiative and collisional components tend to be different. In particular, abundances derived from radiative contribution are systematically higher (by a factor of $\sim$1.5–2.0) than those derived from collisional contribution because of the different weight ascribed to denser regions along the LOS. Hence, our radiative oxygen abundances are closer to the photospheric value. Moreover, we note that more recent oxygen photospheric abundances tend to be lower than older estimates [see, e.g., $\log N(\mathrm{O})_{\mathrm{phot}} \simeq 8.65$; Asplund et al. 2004]: in this case, our oxygen CS underabundance may disappear. Hence, the presence of a FIP effect cannot be unambiguously established for the high-FIP element of oxygen.

On the contrary, the abundance of low-FIP elements like Fe and Si can be evaluated both in the quiet corona and in the CS because a significant fraction of the total line emission originates in the CS itself. Figure 12 (*top right*) shows Fe to be overabundant with respect to its photospheric value both in the quiet corona and in the CS. The CS Fe abundance is only slightly higher than the quiet corona abundance; hence, this difference is within the error bars. However, because this seems to be a persistent feature throughout the data sets until $\sim$18:00 UT of November 28, it is likely to represent a property of the CS plasma, possibly disappearing with time. This overabundance of low-FIP elements is better seen in Figure 12 (*bottom left*), where the CS Si abundance turns out to be about a factor of 5 greater than its photospheric value. Also, the CS Ca turns out to be overabundant by a factor of $\sim$2 with respect to its photospheric value. An enhanced abundance of low-FIP elements in the CS has been found also by Ciaravella et al. (2002) and Ko et al. (2003) and appears to be one of the distinctive properties of CS plasmas.

4.3. *Electron Density Diagnostics*

In order to derive densities, we need to know the values of the quiet corona and CS thickness along the LOS (respectively, L and l). Conversely, knowing abundances and densities, it is easy to derive L-values from the $E_{\mathrm{el}} = A_{\mathrm{el}} n_e n_{\mathrm{H}} L$ relationship (the determination of the quiet corona n_e is explained later in this section). Because in the CS we do not have a means to derive separately l or n_e, we assume the CS thickness to be on the order

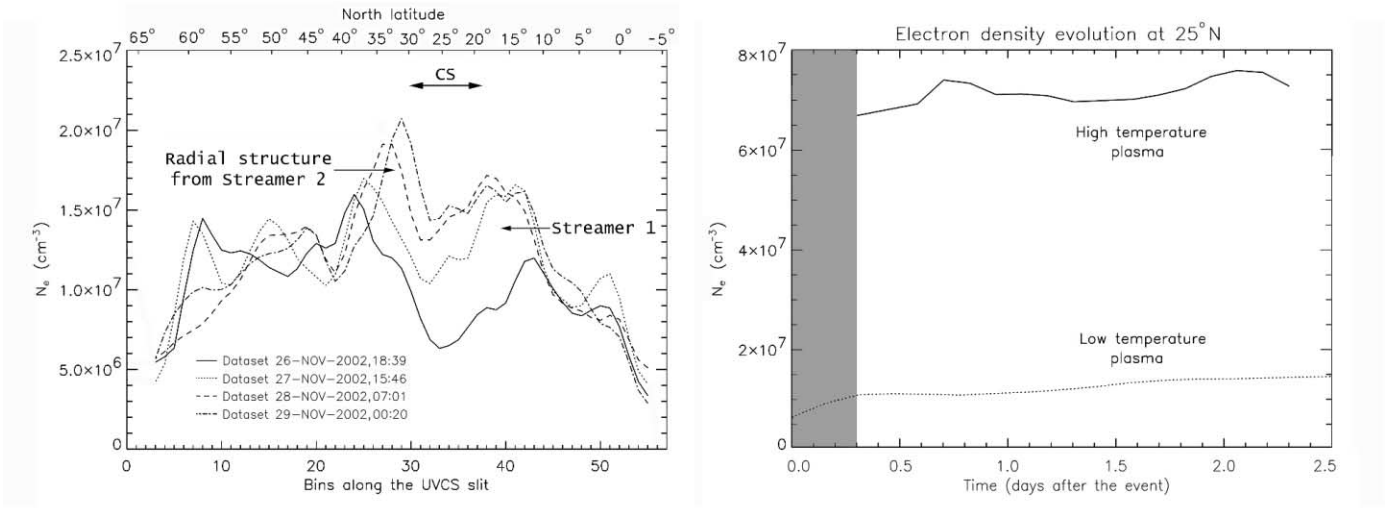

FIG. 13.—*Left*: Densities of the quiet corona along the UVCS slit at different times. *Right*: Temporal evolution of the density at the CS position. The solid line refers to the CS density, and the dotted line refers to the density of the low-temperature plasma in front/behind the CS (see left panel). A gray region covers times when uncertainties are too high to give reliable CS densities.

of $\approx 10^4$ km. Given the observed intensity of the [Fe XVIII] spectral line, the derived temperature T_e, the Fe abundance, and the CS thickness l, we derived representative n_e values in the CS, with an error of a factor of 10 in l implying a factor of 3 error in the derived value of n_e. Figure 12 (*bottom right*) shows that the length of the emitting plasma along the LOS is on the order of half a solar radius, with fluctuations within the error of our estimate. Hence, there is a ratio of order 40 between the quiet corona and the CS emitting length.

We have determined the quiet corona densities from the ratio between the collisional and the radiative components of the O VI λ1032 line intensity that depend, respectively, on n_e^2 and n_e: hence, the ratio θ between the two components turns out to depend on n_e. Because the O VI emission originates only from the ambient corona (§ 4.1.1), densities derived with this method are representative only of the quiet corona and the evaluation is not affected by the presence of the CS. Knowing densities, we calculated the quiet corona thickness L. Following Noci et al. (1987), we write (in cgs units):

$$\theta = (5.75 \times 10^2) \frac{\lambda_{13}^2 e^{(E_{13}/kT_e)} \sqrt{T_e} \int_{13} I_{\rm ex}(\lambda)\, d\lambda}{\bar{g} n_e (\Delta\lambda_{\rm cor}^2 + \Delta\lambda_{\rm ex}^2)^{1/2}} \frac{\Omega}{\pi}, \qquad (4)$$

where $\lambda_{13} = 1031.91$ Å is the wavelength of the transition between the ground and upper levels from which the O VI $\lambda\lambda$1031.9, 1037.6 doublet lines originate, $E_{13} = 1.9251 \times 10^{-11}$ ergs is the energy difference between these levels (k is the Boltzmann constant), $I_{\rm chrom} = \int_{13} I_{\rm ex}(\lambda)\, d\lambda$ is the intensity of the chromospheric exciting line, which has a $1/e$ half-width $\Delta\lambda_{\rm ex} = 0.10$ Å, $\Delta\lambda_{\rm cor} = 0.11$ Å is the $1/e$ half-width of the coronal absorption profile, $\bar{g} = 1.13$ is the Gaunt factor, and Ω is the solid angle subtended by the solar disk.

The separation between the radiative and collisional components has been performed using the same standard procedure followed for the Lyβ and Lyγ lines. Densities derived via equation (4) are crudely evaluated, as a static plasma is assumed and the emission is supposed to originate in the plane of the sky. Plasma along the LOS appears to be static or to have a negligible speed because spectral lines do not show evidence of any shift in λ—that is, no motion along the LOS has been revealed—and the ratio between the 1032 and 1037 Å O VI line intensities is, throughout our data set, on the order of 2.8–3.5. This ratio is indicative of motions in the radial direction: crudely, we can say that a ratio of order $\approx$2 corresponds to an outflow speed of about 100 km s^{-1} (Noci et al. 1987). Higher ratios, such as those in our data set, indicate negligible outflow speeds and justify the technique used to derive densities in the quiet corona (we note that outflows in the CS cannot be inferred from the Doppler dimming of oxygen lines because the O VI emission originates entirely in the quiet corona; see § 4.1.1).

As shown in Figure 8, the Si XII λ499 line is emitted (analogously to the Fe XV λ481 line) both from the low-temperature plasma at $\approx 10^6$ K and from the high-temperature plasma beyond 10^6 K. To separate the two contributions, we followed the same procedure that is described for the Fe XV line and shown in the Appendix.

4.3.1. *Densities in the Current Sheet and Ambient Corona*

Figure 13 (*left*) shows the behavior of electron densities along the UVCS slit at different times. As we said, these have been derived from the ratio between the collisional and radiative components of the O VI λ1032 line. Because the CS plasma does not contribute to the O VI line emission, densities derived with this method refer to the quiet corona plasma; in particular, at the CS latitudes, these are indicative of the plasma densities along the LOS external to the CS itself. Densities are on the order of 10^7 cm^{-3} and are consistent with values found, for instance, by Bemporad et al. (2003) and are a little higher than those of Gibson et al. (1999), which, however, refer to streamers at solar activity minimum. We note that abundances inferred from the O VI line components depend on the O VI disk intensity, for which we do not have, at the time of our observations, any measurement. Hence, densities can be affected by a systematic error, should our disk estimate be inaccurate. The O VI disk intensity has been estimated assuming a value of $I_{\rm disk}({\rm O\ VI}) = 1.94 \times 10^{13}$ photons cm^{-2} s^{-1} sr^{-1} measured by UVCS in 1996, representative of the disk intensity at the last minimum of solar activity. Taking into account that on 2002 November 26 the solar activity was in the descending phase after the solar maximum of 2000, we

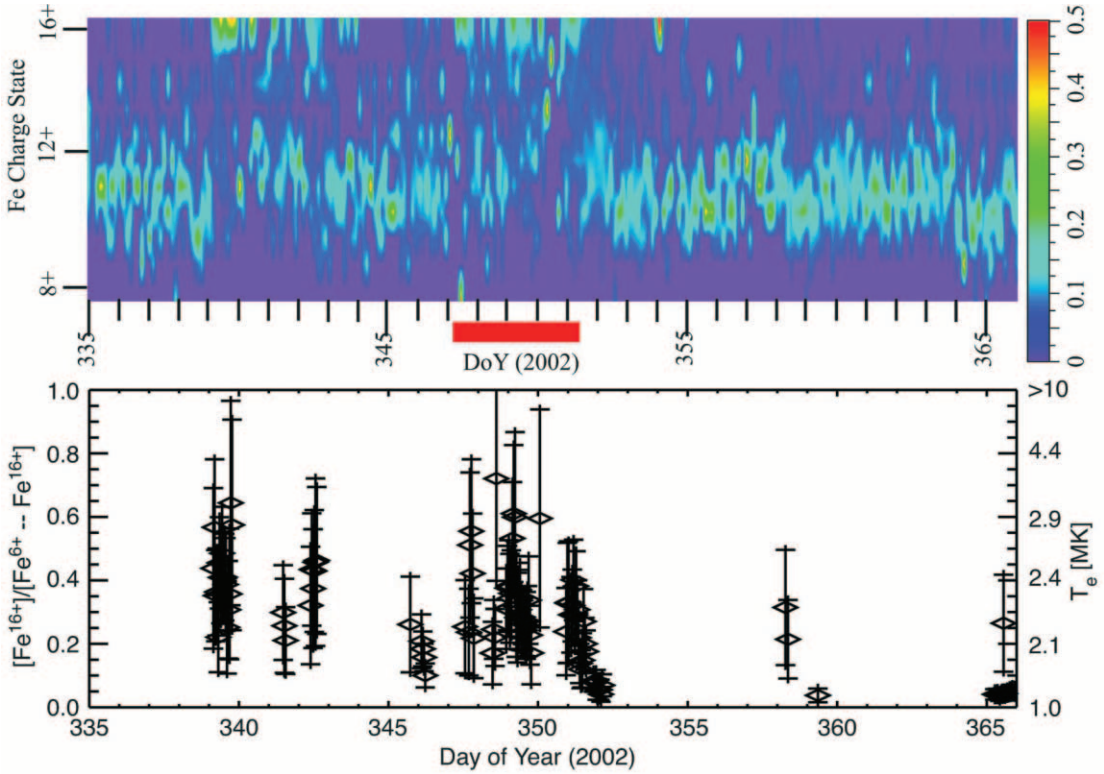

FIG. 14.—Iron charge state vs. day of year (DOY) in 2002 from the *Ulysses* SWICS. *Top*: Colors give the relative abundance of each charge state from 6+ to 16+, with the total abundance normalized to unity for each 3 hr data sample. *Bottom*: Abundance of Fe^{16+} relative to the total abundance of Fe over the range from 6+ to 16+. The red bar below the top panel indicates the interval of enhanced Fe^{16+} that was produced by the November 26 and December 2 CMEs.

used a value of $I_{\rm disk}({\rm O\ VI}) = 3.34 \times 10^{13}$ photons cm^{-2} s^{-1} sr^{-1} from an estimate of the number of ARs at that time using the typical quiet Sun–to–AR ratio given by Vernazza & Reeves (1978).

At the CS latitudes, densities have a minimum, as expected from a corona emptied by the CME ejection. As the CS volume fills up in time, because of the corona restructuring of the northward motion of streamer 1 and of the superposition from northern latitudes of a bright, dense structure onto the CS location (mentioned in § 2), the minimum region decreases in width and tends to disappear. This is more clearly shown in Figure 13 (*right*), where the temporal evolution of the quiet corona in correspondence with the CS is given (*dotted line*). Densities appear to increase by a factor of ≈2.5 over the 2.3 days of observations.

Figure 13 shows (*right panel, solid line*) that the CS density remains constant in time (or possibly increases by no more than 10%) and is 6–8 times greater than that in the adjacent corona. We will discuss later on the behavior of the pressure in the CS; however, it is worth reminding the reader that the CS densities of the figure are only indicative, both because the CS thickness may be greater or smaller than we hypothesized and because we assumed it to be constant in time. As already mentioned, if the thickness of the CS is 1 order of magnitude greater or less than 10^4 km, densities would be a factor of ∼3 lower or higher. Moreover, if the CS is disappearing in time, its thickness l and, as a consequence, its computed densities, will change as well. In conclusion, we can safely assume only that, in the CS, $2 \times 10^7 \leq n_e \leq 2 \times 10^8$ cm^{-3}. We note that, even if the ratio between the quiet corona and CS density is on the order of 0.14, the ratio of order 40 between the quiet corona and the CS emitting length along the LOS justifies the absence of a CS counterpart in the LASCO C2 and C3 white-light images.

5. *ULYSSES* OBSERVATIONS

The measurements by UVCS during and following the November 26 CME showed the creation of high ionization state Fe at 1.7 $R_\odot$ in the aftermath of the CME. Interpreting this in the context of the model illustrated in Figure 1 suggests that the Fe ions flow both up and down along the current sheet. The upward-flowing ions fill a shell inside the boundary of the CME. The question here is whether these Fe ions can be detected at *Ulysses* and, if so, whether the measurements are consistent with the model in Figure 1 and the measurements made by UVCS, LASCO, and EIT described in §§ 2–3. Of particular interest are the *Ulysses* SWICS measurements of Fe and its ionization state, since unusually high ionization state Fe will presumably have been produced in the current sheet between the post-CME loops and the CME that was remotely detected with UVCS. The *Ulysses* SWICS instrument is able to detect Fe from Fe^{6+} through Fe^{16+} (Fe VII–Fe XVII). In 2002 November *Ulysses* was 90° to the west of *SOHO* with respect to the Sun, in quadrature, at a northern heliographic latitude of 27°. This direction is shown by the radial outward line in Figure 2, placing *Ulysses* directly in line with the observed CME, assuming that the CME was at or near the solar limb. The results discussed in §§ 2–3 present a strong argument that the CME was on the limb.

SWICS measurements for several days around 2002 December 13 (day of year [DOY] 347) are shown in Figure 14. Figure 14 (*top*) is a color plot of flux in individual Fe charge states versus time, normalized to a total flux of unity for each 3 hr data sample. It is important to note that the normal charge

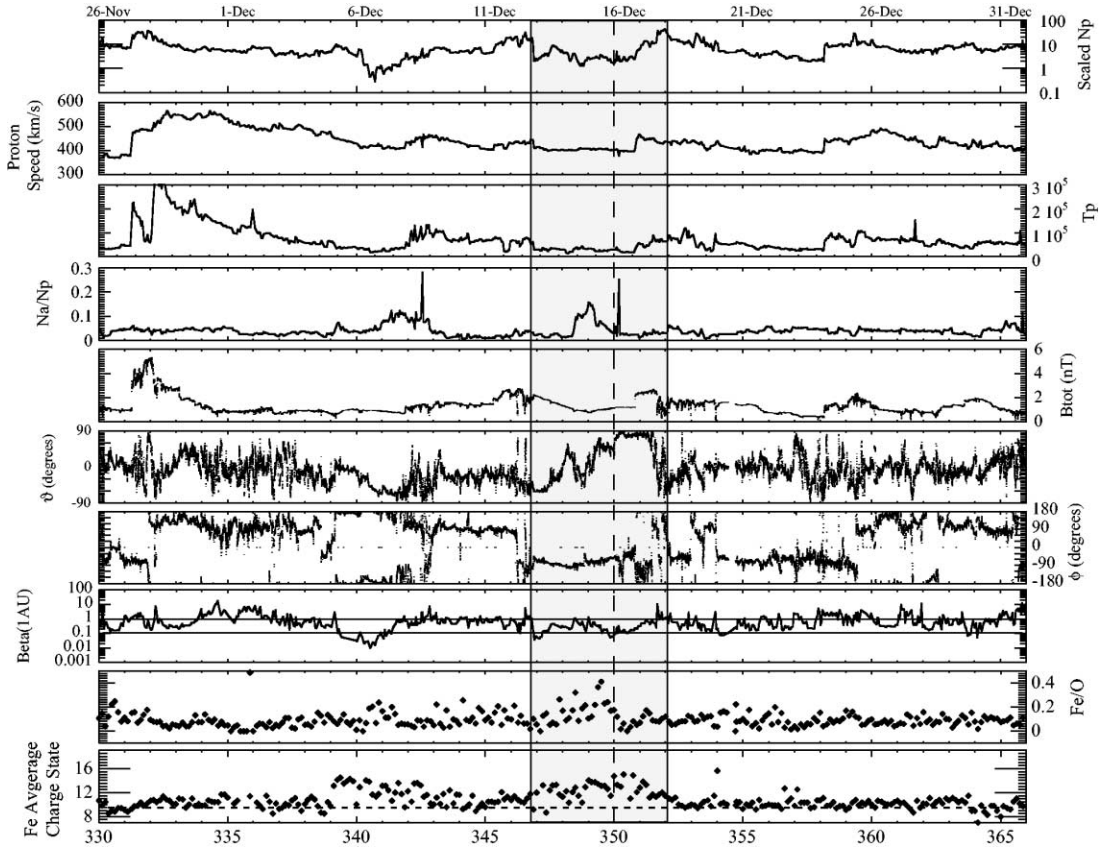

FIG. 15.—Stack plot of the indicated solar wind parameters vs. time over the interval DOY 330–365 in 2002. The proton number density (in cm^{-3}) has been scaled with the inverse square of heliocentric distance to 1 AU. Here β is the ratio of thermal to magnetic pressures, θ is the north-south magnetic field angle, ϕ is the east-west angle, *Btot* is the total magnetic field strength in nT, *Na* is the alpha particle number density, and *Tp* is the proton temperature (K). The gray region bracketed by vertical lines delimits the MIR containing the November 26 CME.

state of Fe in the solar wind is ~10 (Fe XI), and this is precisely what was observed over most of the displayed 30 day period. However, there are also two obvious intervals of high ionization state Fe roughly on DOY 339–344 and DOY 347–352. These intervals cover interaction regions formed by the merging of interplanetary CMEs (ICMEs), commonly known as merged interaction regions (MIRs; Burlaga & Ness 1994). High ionization state Fe is observed in at least one-third of all ICMEs (Lepri et al. 2001; Lepri & Zurbuchen 2004), and these are obvious examples of a positive detection.

Figure 14 (*bottom*) gives the ratio of flux in Fe XVII to the total Fe flux in Fe VII–Fe XVII. All data with Poisson errors greater than 65% have been rejected; the Arnaud & Rothenflug (1985) ionization equilibria have been used to infer temperatures. Because of the ion freezing-in, we can expect these to provide information on the temperatures of the source region of Fe^{16+} ions. As usual, the charge composition data of our event are, however, not isothermal, because unusually high temperatures mix with lower temperatures. This highly structured behavior suggests that we are observing at any given time plasma from many different source regions.

Poletto et al. (2004) extrapolated *Ulysses* measurements back to the Sun using the in situ flow speed measured by SWOOPS, the solar wind plasma detector. This gave a rough estimate of the origin time for the plasma. Then a positive identification of the plasma resulting from the November 26 CME was made by comparing features in the solar wind with phenomena directed toward *Ulysses* in the corona. This was aided by additional CMEs on November 19 and 24 and December 2. Ejecta from the four CMEs was easily identified at *Ulysses* using the results shown in Figure 14 and several other standard markers, including bidirectional streaming of 100 keV electrons, the presence of magnetic clouds, and enhanced alpha-particle abundance. The ICME from the November 26 CME is the first of two CMEs that resulted in the MIR marked with the red bar at the bottom of the top panel in Figure 14, on DOY 347–352.

Figure 15 shows several solar wind parameters on DOY 330–365 that are used to separate the November 26 ejecta from those from the following CME and for comparison with the *SOHO* observations and Figure 1. The panels show, from top to bottom, proton number density scaled inversely with the square of heliocentric distance to 1 AU, proton flow speed, proton temperature, ratio of alpha particle to proton number density, total magnetic field strength, the north-south (θ) and east-west (ϕ) magnetic field angles, the total plasma β, the Fe/O abundance ratio, and the average Fe charge state. These are from the SWOOPS (1 hr data), MAG (1 minute data), and SWICS (3 hr data) instruments. Of these, only the flow speed and the proton density are not used as identifiers of ICMEs, and this is because well inside 2–3 AU dynamic interactions reduce flow speed and density differentials and shift speed patterns with respect to the actual ejecta.

The MIR containing the November 26 CME is bracketed by vertical lines (Fig. 15, *shaded region*). The MIR has the typical ICME properties of low proton temperature, enhanced relative alpha-particle abundance, smooth magnetic field intensity,

rotations of the magnetic field vector, low β-value, enhanced Fe/O, and enhanced Fe average charge state through at least some portion of DOY 347–352.

The rotation of the magnetic field vector, accompanied by low β-value and a smooth magnetic field intensity, is a clear indication of a magnetic cloud (Klein & Burlaga 1982). In the shaded region there is one magnetic cloud between the first vertical solid line and the vertical dashed line. At the dashed line, the rotation changes its behavior, and this probably marks the beginning of the second ICME. Within the second ICME, there is another change at DOY 351, but this is due to the presence of a shock (see the proton flow speed) and is of no significance. There is a drop in Fe/O at DOY 350 that seems to accompany the boundary between the two ICMEs.

Interpreting this in the context of Figure 1 is straightforward. There are two important properties of this model to look for in the data. The first is the presence of Fe XVII at both the back and the front of the ICME, even though it has been generated in the corona in the aftermath of the CME. Here we see that there is not only Fe XVII at the front and back of the ICME, independent of where we pick the boundary between the two ICMEs, but also more or less throughout the ICME. In the context of Figure 1, this could mean that *Ulysses* did not pass through the center of the ICME or magnetic cloud, but rather off center, so that its trajectory missed the void. Alternatively, the void could have been very small or absent. The first interpretation is supported by the magnetic field rotation in the cloud, which is not either a simple $90^\circ \rightarrow 0^\circ \rightarrow -90^\circ$ rotation in θ or a $180^\circ \rightarrow 0^\circ \rightarrow -180^\circ$ rotation in ϕ. Instead, the rotation is less than a full circle. Thus, we believe that the field rotation in the magnetic cloud and the observed enhanced Fe ionization state throughout the magnetic cloud are support for the conclusion that the observed ICME had the properties predicted from Figure 1 and that *Ulysses* passed through the edge of the ICME.

The SWICS data in Figure 14 (*bottom*) exhibit strong fluctuations in ionization state that are not being resolved. This explains why inferred temperatures are less than the >6 MK inferred in the corona using UVCS. This apparently filamentary structure is not present in the magnetic field, which has the typical relatively smooth structure of a magnetic cloud. Figure 15 shows this point by the strong field strength fluctuations outside the ICME in comparison to the near absence of such fluctuations inside the ICME. The explanation for the charge state fluctuations in the absence of magnetic field fluctuations is, as stated above, that the Fe must come from many different source regions. The reconnection between the CME and the post-flare loops that forms the outer shell around the CME shown in Figure 1 must be patchy, bursty, and localized, as is often the case in reconnection observed elsewhere in space plasmas. The different ionization Fe states, which flow up and around the CME, have been created by reconnection in different source regions at different times. In this scenario, essentially all field lines reconnect to form the smooth outer shell of the magnetic cloud, but the structured history of each field line is reflected in the structure of the Fe ionization state.

In a recent paper Grigis & Benz (2005) report *RHESSI* (*Reuven Ramaty High-Energy Solar Spectroscopic Imager*) direct observations of reconnection along an arcade of magnetic loops similar to the EIT arcade previously described here. They interpret their data, which show many distinct X-ray emission peaks at different times, as evidence of "elementary flare bursts"; that is, as evidence of reconnection processes that progress irregularly along the arcade. *Ulysses* observations of highly fluctuating Fe ionization states may represent the interplanetary imprint of such reconnection pattern, even if we are obviously unable to trace individual data back to the precise location where reconnection is occurring in the corona. EIT data, however, support this interpretation, as the location of the brightest loop changes in time.

6. DISCUSSION AND CONCLUSIONS

The propagation of a CME in the solar atmosphere has been studied by Lin (2002), who found that the average Alfvén Mach number for the inflow into the reconnection site (i.e., the velocity of plasma flowing into the reconnection site in units of the local Alfvén speed) needs to be larger than 0.013 in order to allow the flux rope to escape into the interplanetary space. Direct measurements of the plasma inflows are extremely scanty. Yokoyama et al. (2001) gave an upper limit of 5 km s^{-1} for the inflows around an X-type neutral point over flare loops, while Lin et al. (2005) gave values ranging between 10.5 and 106 km s^{-1} for inflows near the CS in a fast CME event (velocities on the order of 1500–2000 km s^{-1} for the leading edge/core of the CME). The latter values refer to measurements taken over 10 minutes at the beginning of the CME event and are likely to decrease as the event evolves.

There is no possibility to detect in our spectra such low velocities, because the corresponding Doppler shift is too small. Nevertheless, we tried to get some information about inflows and magnetic fields in the reconnection region by parameterizing inflow values and identifying those that give reasonable values of the magnetic field $B_{\rm in}$ in the corona adjacent to the CS. To this end we write the equations (in cgs units) for pressure equilibrium and mass conservation across the CS. If the external plasma ($p_{\rm in}$, $\rho_{\rm in}$) is flowing into the CS with a speed $v_{\rm in}$, carrying in a magnetic field $B_{\rm in}$, we can write

$$p_{\rm in} + \frac{1}{2}\rho_{\rm in} v_{\rm in}^2 + \frac{B_{\rm in}^2}{8\pi} = p_0 + \frac{1}{2}\rho_0 v_0^2, \tag{5}$$

$$\rho_{\rm in} v_{\rm in} h = \rho_0 v_0 l, \tag{6}$$

where p_0 and ρ_0 are, respectively, the plasma pressure and density of the CS, where B_0 is negligible, and v_0 is the speed of the plasma flowing out of the top and bottom of the CS toward, respectively, interplanetary space and the chromosphere. The CS is assumed to have a width l along the LOS and to extend radially over a characteristic length h.

If we assume $v_{\rm in}$ to take values between 10 and 100 km s^{-1}, h to have a characteristic value of $\approx 1\ R_\odot$, and l to be on the order of 10^4 km, as previously assumed, we can solve equations (5) and (6) for $B_{\rm in}$ and v_0, as all other quantities have been derived from observations. Hence, we prescribed constant values of $v_{\rm in}$ and solved the equations for the unknown quantities over the whole time interval of our observations. Results for $M_{\rm A}$ and $B_{\rm in}$ versus time are shown in Figure 16.

Figure 16 shows that inflow speeds $\leq$10 km s^{-1} correspond to $M_{\rm A}$ numbers that are too low to allow the CME to be ejected into the interplanetary space; hence, they are seemingly not realistic. On the other hand, inflows as high as 100 km s^{-1} give magnetic field values increasing with time, a tendency shown very mildly also in the $B_{\rm in}$ versus time profile for values of $v_{\rm in}$ of 50 km s^{-1}. Considering that the CS is eventually disappearing, as revealed by the fading emission in [Fe XVIII], an increase of $B_{\rm in}$ seems unrealistic, and we are drawn to discard solutions for which this happens. Moreover, we point out that the $M_{\rm A}$ curve shown in Figure 16 with $v_{\rm in} = 100$ km s^{-1} is above 0.03, which seems to be the $M_{\rm A}$

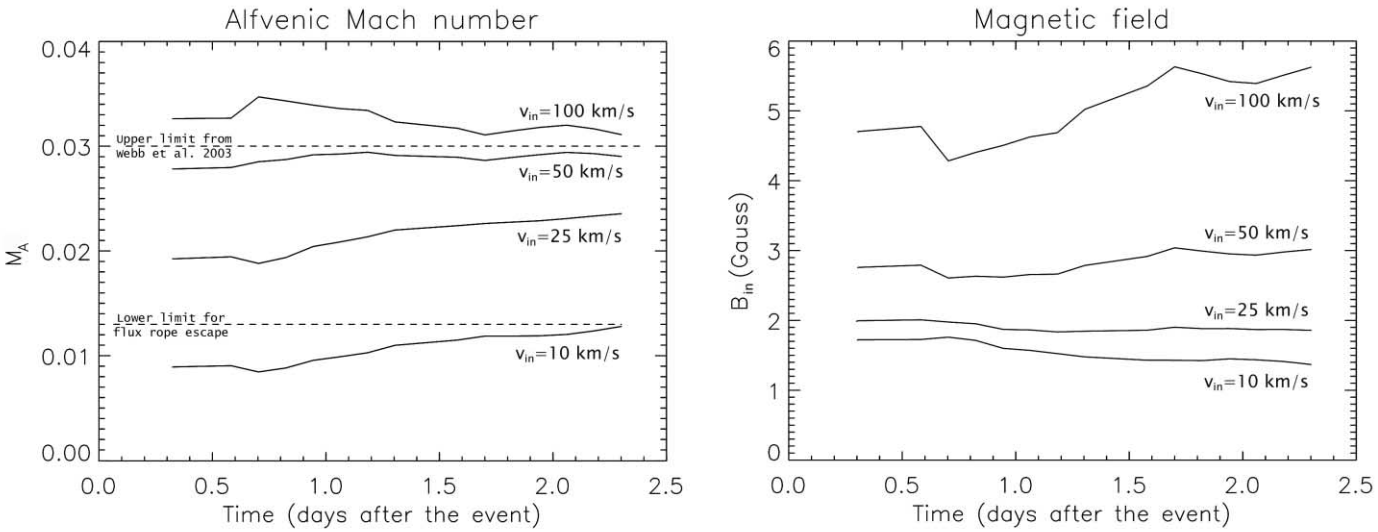

FIG. 16.—*Left*: Temporal profile of the Alfvénic Mach number M_A for different values of inflow velocities. The bottom dashed horizontal line gives the threshold value of M_A that still allows the CME to escape from the solar atmosphere. *Right*: Temporal profile of the magnetic field B_{in} in the inflow region for the inflows adopted in the left panel. No values are given for times when physical parameters have not been evaluated (gray regions in Figs. 13 and 11).

peak value reached tens of minutes after the event (Webb et al. 2003). We conclude that inflows toward the reconnection region should be higher than 10 km s^{-1} but lower than 50–100 km s^{-1}. This result points to slightly higher values than those found by Yokoyama et al. (2001) and indicates that the inflow pattern should persist over the whole lifetime of the CS, as might be expected.

From the previous inflow values, the speed of the plasma outflows from the CS turns out to vary from $v_0 \approx 100$ km s^{-1} for inflows of 10 km s^{-1} to outflows 10 times larger for inflows of 100 km s^{-1}. These values give lower and upper limits for outflows: if we had the possibility of observing the Doppler dimming effect, we might test our conclusions. However, Ko et al. (2003) and Lin et al. (2005) gave estimates of the outflow speed by measuring the height versus time profile of LASCO blobs seen at altitudes larger than 2 $R_\odot$. These authors give speeds of 500–1000 km s^{-1}, which are consistent with our values, considering that our CME was a slower event than the CMEs analyzed by Ko et al. (2003) and Lin et al. (2005).

Inflows toward the CS region may provide for heating the CS by adiabatic compression. However, no conclusion has been reached yet on whether this process or ohmic heating by reconnection (not to mention other heating mechanisms, such as, for instance, slow-mode shocks) can account for the high temperatures in the CS. On the basis of the plasma parameters we derived, we have the possibility of checking on this issue by comparing the quiet corona with the CS plasma. In the case in which the external plasma undergoes an adiabatic compression flowing into the CS, we expect

$$\frac{T_0}{T_{\rm in}} = \left(\frac{N_{e,0}}{N_{e,\,\rm in}}\right)^{\gamma-1},$$

where T_0 and $T_{\rm in}$ are, respectively, the CS and quiet corona temperature, while $N_{e,0}$ and $N_{e,\,\rm in}$ are the corresponding electron densities. The plot in Figure 17 appears to indicate that at a late stage of the event, adiabatic compression can provide for the high CS temperatures, while at earlier times other processes should be invoked. This is not unreasonable, as the CS erosion is likely to result in a reduced ohmic heating. This result holds as long as the CS thickness of 10^4 km assumed so far is constant in time.

Figure 17 shows that, ≈2 days after the event, temperature and density in the CS are still higher than ambient values. This is obviously confirmed by Figure 6, where emission from the [Fe XVIII] ion, typical of the CS, has not faded yet at the end of the UVCS observations. This evidence points to a CS lifetime longer than 2 days. This duration is not uncommon for CSs detected by UVCS: for instance, in Ciaravella et al. (2002) and Ko et al. (2003), CSs are observed to last for ≥1 day. Prior to these observations, the duration of reconnection processes was usually

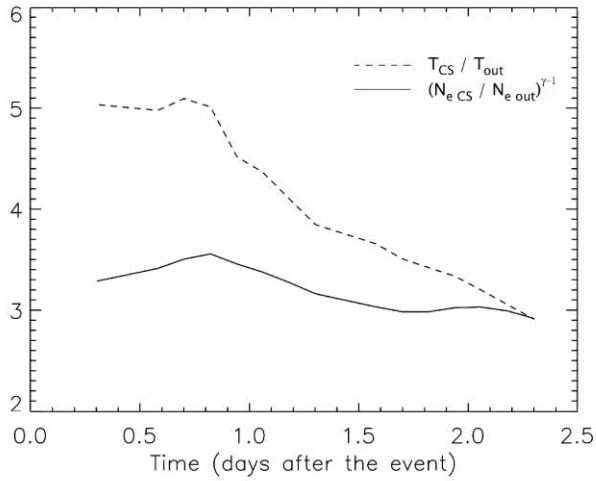

FIG. 17.—Temporal profile of the observed ratio of the CS temperature to the quiet corona temperature (*dotted line*) compared to the ratio inferred from the observed densities under the assumption of an adiabatic compression of the plasma (*solid line*).

inferred from either the time over which chromospheric ribbons kept separating or the time over which hot loops kept rising to higher altitudes. From the time history of the Hα ribbon separation and of the hot loop heights for the 1973 July 29 flare that was considered to be an ideal example for a case study (see, e.g., Moore et al. 1980; Svestka et al. 1982), reconnection was recognized to go on for at least $\approx$10 hr. Hence, UVCS data considerably extended the time interval over which reconnection was observed to operate.

It is interesting to check on the duration of reconnection processes in theoretical models. Lin (2002) has pointed out the influence of the ambient corona in the evolutionary behavior of the CS. The isothermal atmosphere he first used in his model was superseded in his later simulations by the Sittler & Guhathakurta (1999) empirical atmosphere, based on *Skylab* White Light Coronagraph observations and in situ *Ulysses* data. Because in Sittler & Guhathakurta (1999) the Alfvén speed keeps decreasing with height, the CS is not rapidly eroded and its persistence over $\approx$1 day is easily predicted. Also, Lin (2002) showed how a weak background field slows down the rise of the CME and how the morphology of the field, whether it is compacted in a small region or not, sensibly affects the motion of the flare ribbons. Hence, while qualitatively we can say that the lifetime of the CS inferred in our work can be consistent with predictions from the Lin & Forbes (2000) model, observations of the magnetic field and a better knowledge of the ambient atmosphere is needed to be able to simulate theoretically results inferred from UVCS observations. To our knowledge, this is a relevant issue that has not yet been fully explored.

Throughout this work we have been assuming ionization equilibrium. To check whether this is a realistic assumption, we computed collisional ionization and autoionization rates and radiative and dielectronic recombination rates, as a function of time, for transitions between Fe XIV and Fe XV and between Fe XVII and Fe XVIII. We selected these ions because they are those from which we calculated the electron temperatures and, as a consequence, the other parameters in the CS. Over the range of temperatures covered by our data, the highest rates are those for dielectronic recombination processes, which are on the order of a few times 10^{-11} cm^3 s^{-1}. At the beginning of our observations, with $T_0 \approx 8\times10^6$ K, $N_{e,0} \approx 6.5\times10^7$ cm^{-3} recombination times are on the order of 500 s. Plasma flowing into the current sheet at $\approx$20 km s^{-1} crosses a 10^4 km CS in about $\approx$500 s: hence, we can roughly assume that atomic processes occur over characteristic times comparable with the time that the plasma takes to cross the CS. Analogously, at the end of the observations, when inflows are, say, 10 times slower than at the beginning of the event, the plasma crossing time is 10 times longer, and dielectronic recombination times (for $T_0 \approx 4\times10^6$ K and $N_{e,0} \approx 7.5\times10^7$ cm^{-3}) are on the order of 300 s. We conclude that ionization equilibrium seems to hold throughout the CS lifetime: we also point out that the CS cooling seems to occur on a longer timescale than the $\approx$5–10 minute timescale of atomic processes.

With regard to *Ulysses* measurements, the ICME resulting from the November 26 CME was already identified by Poletto et al. (2004). Here a closer examination of that ICME was carried out by examining the full set of measurements made by SWOOPS, MAG, and SWICS. These data are shown in Figures 14 and 15. The data permitted separating the two ICMEs in the MIR on DOY 347–353 through examination of magnetic field rotations in the magnetic cloud. This separation was not unique, but the interpretation was independent of this. The interpretation led to the conclusion that the Fe ionization state was elevated, with strong fluctuations, from $\sim$10+ to $\sim$16+ throughout the entire ICME produced by the November 26 CME. This implies both that the model shown in Figure 1 fits the in situ observations and that *Ulysses* passed through the edge of the resulting ICME rather than the center. The fluctuations in the Fe ionization state, together with a smooth magnetic field, suggest that the reconnection in the coronal current sheet that produced the Fe XVII was filamentary and bursty.

We summarize the main results of this paper as follows:

1. Analysis of a unique *SOHO*-*Ulysses* data set allowed us to describe the structure of a CS, which formed in the aftermath of a coronal mass ejection, from lower coronal levels out to interplanetary distances.
2. We derived the physical parameters of this CS over 2.3 days following the event. In particular, after separating the quiet corona and CS contributions to the plasma emission along the line of sight, we derived the temporal profile of the CS temperature, density, and elemental abundances. We showed that the CS temperature decreases by more than a factor of 2 over the observing time. The behavior of the density is not as well defined, due to the superposition of a dense feature onto the CS location at the end of our observations. Low-FIP elements appear to be overabundant with respect to their photospheric values.
3. A range of values for the plasma inflow speed toward the reconnection has been inferred, together with values of the magnetic field in the reconnection region.
4. We showed that adiabatic compression of plasma cannot account for the heating of the reconnection region, other than at a very late phase of the phenomenon.
5. The resulting ICME is consistent with the model displayed in Figure 1.
6. Strong fluctuations in the high-ionization Fe states detected in situ suggest bursty rather than smooth reconnection in the coronal CS and have been related to the irregular progression of reconnection events along the arcade of post-event loops.

G. P. is grateful to T. Forbes, R. Moore, A. Sterling, D. Falconer, and G. Noci for useful discussions. We thank J. Lin for his comments on a first version of this paper and for making Figure 1 available to us. *SOHO* and *Ulysses* are missions of international cooperation between ESA and NASA. G. P. acknowledges support from contract COFIN 2003029124003. S. T. S. acknowledges support of *Ulysses* SWOOPS and the *Ulysses* project.

APPENDIX

We give in Figure 18 a "flowchart" that shows how different parameters have been evaluated. Figure 18 (*left*) refers to the "quiet," low-temperature plasma, and Figure 18 (*right*) refers to the CS, high-temperature plasma. At the latitude of the CS, both regions contribute along the LOS to the observed line intensities; at the latitudes beside the CS, only the quiet coronal emission is present. The flowchart illustrates the mutual relationships among different parameters.

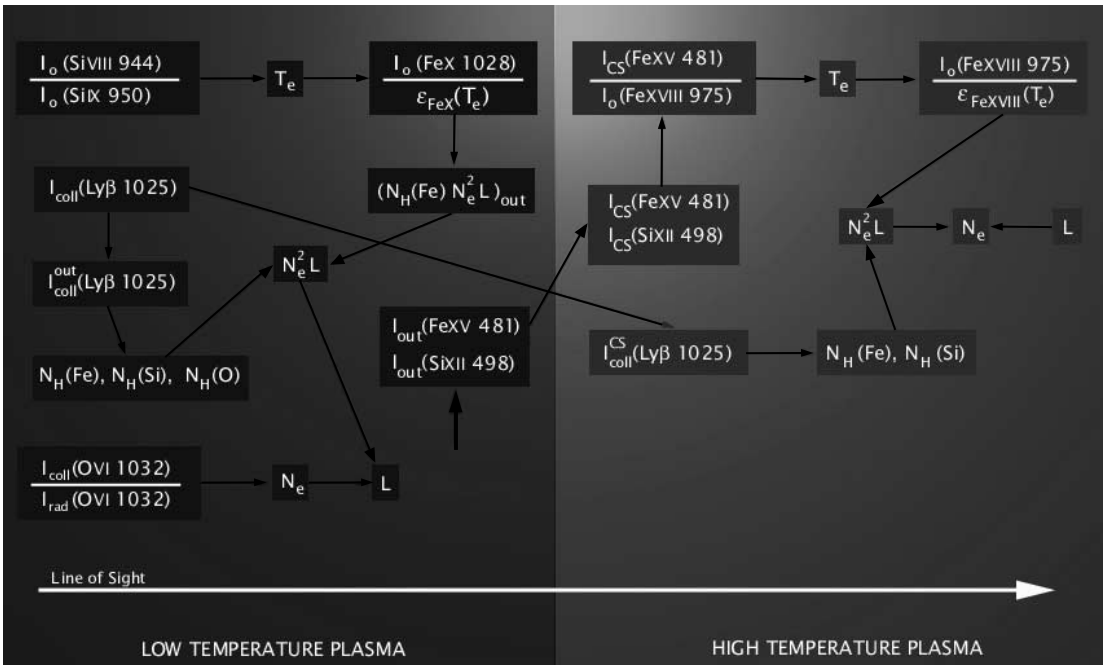

FIG. 18.—Flowchart diagram showing the procedure used in the paper to separate the contributions along the LOS of the high-temperature CS and the quiet corona to the line intensities and to determine the plasma physical parameters of both regions.

REFERENCES

Allen, C. W. 1973, Astrophysical Quantities (3rd ed.; London: Athlone)
Antiochos, S. K., DeVore, C. R., & Klimchuk, J. A. 1999, ApJ, 510, 485
Arnaud, M., & Rothenflug, R. 1985, A&AS, 60, 425
Asplund, M., Grevesse, N., Sauval, A. J., Allende Prieto, C., & Kiselman, D. 2004, A&A, 417, 751
Bemporad, A., Moore, R. T., Sterling, A., & Poletto, G. 2005, ApJ, submitted
Bemporad, A., Poletto, G., Suess, S. T., Ko, Y.-K., Parenti, S., Riley, P., Romoli, M., & Zurbuchen, T. Z. 2003, ApJ, 593, 1146
Brueckner, G. E., et al. 1995, Sol. Phys., 162, 357
Burlaga, L. F., & Ness, N. F. 1994, J. Geophys. Res., 99, 19341
Ciaravella, A., Raymond, J. C., Li, J., Reiser, P., Gardner, L. D., Ko, Y.-K., & Fineschi, S. 2002, ApJ, 575, 1116
Delaboudinière, J.-P., et al. 1995, Sol. Phys., 162, 291
Foley, C. R., Patsourakos, S., Culhane, J. L., & MacKay, D. 2002, A&A, 381, 1049
Gibson, S. E., Fludra, A., Bagenal, F., Biesecker, D., Del Zanna, G., & Bromage, B. 1999, J. Geophys. Res., 104, 9691
Grigis, P. C., & Benz, A. O. 2005, A&A, 434, 1173
Klein, L. W., & Burlaga, L. F. 1982, J. Geophys. Res., 87, 613
Ko, Y.-K., Raymond, J. C., Lin, J., Lawrence, G., Li, J., & Fludra, A. 2003, ApJ, 594, 1068
Kohl, J. L., et al. 1995, Sol. Phys., 162, 313
Lepri, S. T., & Zurbuchen, T. H. 2004, J. Geophys. Res., 109, 1112
Lepri, S. T., Zurbuchen, T. H., Fisk, L. A., Richardson, I. G., Cane, H. V., & Gloeckler, G. 2001, J. Geophys. Res., 106, 29231
Lin, J. 2002, Chinese J. Astron. Astrophys., 2, 539
Lin, J., & Forbes, T. G. 2000, J. Geophys. Res., 105, 2375
Lin, J., Ko, Y.-K., Sui, L., Raymond, J. C., Stenborg, G. A., Jiang, Y., Zhao, S., & Mancuso, S. 2005, ApJ, 622, 1251
Mazzotta, P., Mazzitelli, G., Colafrancesco, S., & Vittorio, N. 1998, A&AS, 133, 403
Mikić, Z., & Linker, J. A. 1994, ApJ, 430, 898
Moore, R. L., LaRosa, T. N., & Orwig, L. E. 1995, ApJ, 438, 985
Moore, R. L., et al. 1980, in Solar Flares: A Monograph from Skylab Solar Workshop II, ed. P. A. Sturrock (Boulder: Colorado Assoc. Univ. Press), 341
Noci, G., Kohl, J. L., & Withbroe, G. L. 1987, ApJ, 315, 706
Parenti, S., Bromage, B. J. I., Poletto, G., Noci, G., Raymond, J. C., & Bromage, G. E. 2000, A&A, 363, 800
Poletto, G., Suess, S. T., Bemporad, A., Schwadron, N. A., Elliott, H. A., Zurbuchen, T. H., & Ko, Y.-K. 2004, ApJ, 613, L173
Raymond, J. C., Ciaravella, A., Dobrzycka, D., Strachan, L., Ko, Y.-K., Uzzo, M., & Raouafi, N.-E. 2003, ApJ, 597, 1106
Raymond, J. C., et al. 1997, Sol. Phys., 175, 645
Scherrer, P. H., et al. 1995, Sol. Phys., 162, 129
Sittler, E. C., Jr., & Guhathakurta, M. 1999, ApJ, 523, 812
Sturrock, P. A., Kaufman, P., Moore, R. L., & Smith, D. F. 1984, Sol. Phys., 94, 341
Svestka, Z., Dodson-Prine, H. W., Martin, S. F., Mohler, O. C., Moore, R. L., Nolte, J. T., & Petrasso, R. D. 1982, Sol. Phys., 78, 271
Uzzo, M., Ko, Y.-K., & Raymond, J. C. 2004, ApJ, 603, 760
Uzzo, M., Ko, Y.-K., Raymond, J. C., Wurz, P., & Ipavich, F. M. 2003, ApJ, 585, 1062
Vernazza, J., & Reeves, E. M. 1978, ApJS, 37, 485
Webb, D. F., Burkepile, J., Forbes, T. G., & Riley, P. 2003, J. Geophys. Res., 108 (A12), 1440, DOI: 10.1029/2003JA009923
Yokoyama, T., Akita, K., Morimoto, T., Inoue, K., & Newmark, J. 2001, ApJ, 546, L69